PREPARATION AND CHARACTERIZATION OF DOPED ZINC OXIDE

by

YOGEESWARAN GANESAN

Presented to the Faculty of the Graduate School of

The University of Texas at Arlington in Partial Fulfillment

of the Requirements

for the Degree of

MASTER OF SCIENCE IN MATERIALS SCIENCE AND ENGINEERING

THE UNIVERSITY OF TEXAS AT ARLINGTON

August 2006

ACKNOWLEDGEMENTS

I would like to start by expressing my sincere thanks to my research advisor, Prof. Krishnan Rajeshwar whose scientific acumen and positive encouragement have guided my research. I am also greatly indebted to Drs. Norma Tacconi and C. R. Chenthamarakshan for their extraordinary guidance during the course of my thesis work.

I would like to thank my committee members, Profs. Yaowu Hao and Michael Jin, for their constructive feedback and stimulating questions. I appreciate the support of Mr. Ashwin Seshadri whose original work on the Zn-Cd-O system laid the foundations for this thesis. Finally, I would like to thank my parents for their constant support and encouragement.

July 24, 2006

ABSTRACT

PREPARATION AND CHARACTERIZATION OF DOPED

ZINC OXIDE

Publication No. _____

Yogeeswaran Ganesan, M.S.

The University of Texas at Arlington, 2006

Supervising Professor: Krishnan Rajeshwar

Cathodic electrodeposition was used to prepare thin films of ZnO doped with Cd, from oxygenated KCl electrolyte containing $ZnCl_2$ and $CdCl_2$ in various molar ratios ranging from 0 mM to 5.0 mM each. Evidence for doping was obtained from X-ray powder diffraction, diffuse reflectance, chronopotentiometry, and X-ray photoelectron spectroscopy data. The Cd-doped ZnO samples showed a superior photoresponse relative to undoped ZnO.

Cadmium- and indium- doped ZnO were prepared by combustion synthesis using $CdCl_2$ and $InCl_3$ as dopant precursors along with zinc nitrate and urea as the combustion mixture. The doped samples were compared and contrasted with undoped ZnO using scanning electron microscopy, X-ray powder diffraction, energy-dispersive

X-ray analyses and X-ray photoelectron spectroscopy. Diffuse reflectance spectroscopy showed the optical bandgap of ZnO to shrink from 3.14 eV to 3.07 eV and 3.02 eV on Cd- and In- doping respectively. The doped samples showed an improved photoelectrochemical response relative to undoped ZnO over the wavelength range from ~300 nm to ~450 nm.

TABLE OF CONTENTS

LIST OF ILLUSTRATIONS

Figure Page

LIST OF TABLES

CHAPTER 1

INTRODUCTION

1.1 Zinc Oxide

ZnO is a II–VI semiconductor with a direct, dipole allowed band gap around 3.2 eV i.e., in the near UV and an exciton binding energy of about 60 meV. ZnO is naturally an n-type semiconductor partially due to its deviation from stoichiometry i.e., due to the presence of interstitial Zn atoms (Zn_i) in large voids and the presence of oxygen vacancies (V_o) in the crystal and partially due to the presence of background donors such as H and Al. These defects form donor levels at ~ 0.05 eV [1].

Intensive research on ZnO bulk samples started gradually in the 1950s and peaked towards the end of the seventies and the beginning of the eighties. The emphasis of the research was on topics such as growth, doping, transport, deep color centers, band-structure, excitons, bulk- and surface-polarons, luminescence, and lasing. The interest faded away for a while partly because it was not possible to achieve p-type doping in ZnO and partly because the interest moved to structures of reduced dimensionality, especially the GaAs/$Al_{1-y}Ga_yAs$ system.

There has been a renaissance of ZnO research in recent times based on the successful achievement of p-type doping in ZnO [1] and on the possibility to grow epitaxial layers, quantum wells, nano-rods, quantum dots and related objects. Much of the renewed interest has been focused on ZnO because it is:

- a material for transparent thin film transistors

- a material for blue/UV lasers, LEDs and other optoelectronic devices in addition to (or instead of) the GaN based structures

- a radiation-hard material for electronic devices in a corresponding environment

- a diluted or ferromagnetic material, when doped with Co, Mn, Fe, V etc., for spintronics

- a transparent, highly conducting oxide (TCO), when doped with/alloyed with Al, Ga, In etc., as a cheaper alternative to indium tin oxide (ITO) [2].

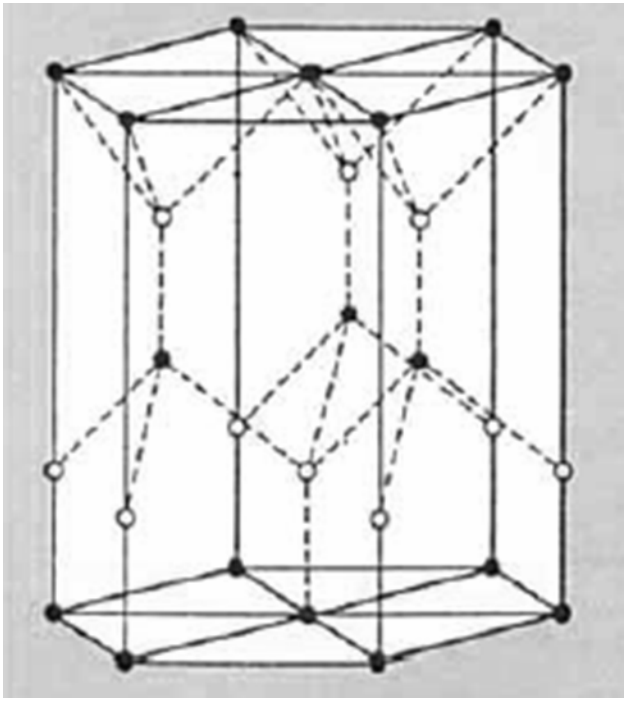

Figure 1.1 The crystal structure of ZnO (shaded circles indicate the positions of oxygen atoms while the open circles indicate the positions of the zinc atoms).

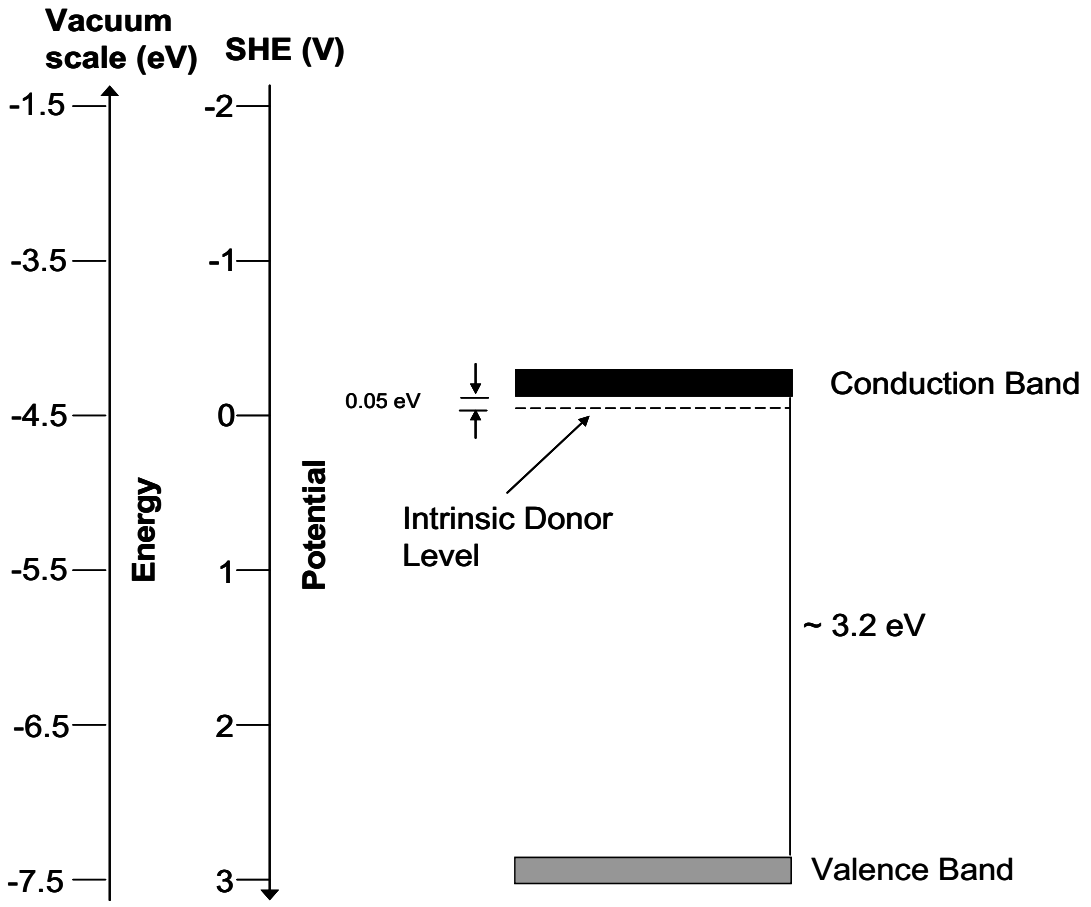

Figure 1.2 Relative dispositions of ZnO band edge positions shown both on the vacuum scale and with respect to standard hydrogen electrode reference. These band positions are for an aqueous medium of pH~1.

1.2 Synthesis of Zinc oxide

It is worth noting that ZnO occupies an enviable place in the industrial market. Tens of thousand tonnes of ZnO powder are industrially produced each year which are used in the rubber industry as a vulcanization activator, in the ceramic industry as a flux, in the chemical industry (desulphurization of gases, fabrication of stearates, phosphates etc.), as trace elements in animal food, in the paint industry and in the electronic industry (ferrites, varistors).

ZnO powder is produced from the combustion of vapors coming from the distillation of metallic zinc according to the so-called 'French' or 'dry' process. Using vapors emanating from the fractionated distillation of Zn, extra pure oxide powder with a Pb content < 20 ppm, a Cd content < 10 ppm, a Fe content < 5 ppm and a Cu content < 1 ppm can be obtained [3].

Single crystals of ZnO can be grown from melts, by chemical vapor transport in closed tubes, from solutions or by hydrothermal methods. The electrical and structural properties of the crystals grown generally remain similar irrespective of the method used for preparation [3].

Thin layers of ZnO have been grown by various techniques including chemical vapor deposition (CVD) [4], pulsed laser deposition (PLD), molecular beam epitaxy (MBE) [5], dc- and rf-magnetron sputtering [6,7], metal organic chemical vapor deposition [8], and electrodeposition [9]. Layer properties are very dependent on the particular method used for film preparation.

1.3 Doping of ZnO

Doping of a semiconductor is defined as the addition of a small percentage of foreign atoms in its regular crystal lattice with the intent of producing dramatic changes in its properties (when large percentages are involved this process is referred to as alloying). Doping is a routine process generally associated with the fabrication of silicon based semiconductor devices. N type doping is achieved when group VA impurity elements such as P, As and Sb get introduced into the silicon lattice, thus providing easily

ionized electrons for electrical conduction. Group IIIA elements such as B and Al act as p-type dopants in silicon since they supply positively charged carriers (holes).

In recent times, ZnO has become an important wide band gap semiconductor with a number of potential applications because of its distinctive properties (wide direct bandgap, a large exciton binding energy, chemical etchability etc.). In the optoelectronic industry, for example, there is a huge demand for materials that can be used in short wavelength devices, as transparent electrodes and as windows for displays and solar cells. However, for any of the aforementioned applications, it is important to control the physical (e.g., the lattice parameters), electronic, (e.g., band gap, conductivity) and optical properties (optical transmission) of the compound, and this can be done via doping. Also, the incorporation of dopants can sometimes lead to the development of some rather unique properties useful for the fabrication of devices. For example, Cd-doped ZnO nanowires prepared by a co-evaporation technique were found to possess a positive coefficient of resistance and humidity-sensing properties [10].

ZnO has a wurtzite structure (see Figure 1.1) in which the oxygen atoms are arranged in a hexagonal close-packed type lattice with zinc atoms occupying half the tetrahedral sites. The two types of atoms, Zn and O, are tetrahedrally coordinated to each other and are therefore equivalent in position. The ZnO structure is thus relatively open with all octahedral sites and half the tetrahedral sites empty. It is therefore relatively easy to incorporate external dopants into the ZnO lattice [11].

There is a vast amount of literature available on the doping of ZnO. ZnO has been doped with a number of elements including Al, Ga, In, B, Si, Ge, Ti, Zr, Hf, Mn, Co, Mg, Li etc., and the properties of the resulting materials have been extensively studied. Past

studies on two of the most common ZnO-based systems will be briefly reviewed in the following sub-sections.

The Zn-In-O system

The Zn-In-O system is one that has been extensively studied in the recent past as a potential material for low-cost transparent electrodes. Nine homologous compounds of $(ZnO)_mIn_2O_3$ composition are known to exist [12]. These polytypes crystallize rhombohedrally or hexagonally with a wurtzite type ZnO block (a_o= 0.325 nm and c_o= 0.521 nm) stacked alternately with a cubic bixbyite-type In_2O_3 layer (a_o= 1.0117 nm). The two structures intergrow along the c axis of the ZnO subcell, as well as the <111> direction of the In_2O_3 subcell [13]. It has been reported that the m=2 polytype exhibits a high optical transmittance with a slightly greater resistance than that of Sn doped In_2O_3 (ITO) [14].

The replacement of a small number of Zn atoms in the ZnO lattice by In, on the other hand, results in the formation of n-type doped ZnO. In the past, research has been focused on the characterization of thin films of the material prepared by simultaneous RF and DC magnetron sputtering, electrodeposition, and spray pyrolysis. Optical studies on electrodeposited In-doped ZnO films have shown that a doping level of 1 at% indium produced films with high conductivity and enhanced optical transmission [15].

The Zn-Cd-O system

Since the first report in 1996 [16], a raft of studies have begun to appear on the Zn-Cd-O material system. This is primarily because alloying with Cd has been identified as an attractive method for engineering the bandgap of ZnO. Thus, the ability to build multilayer structures of ZnO with $Zn_xCd_{1-x}O$ films would facilitate the fabrication of

heterojunctions and quantum well devices. Also, Cd additions can alter the refractive index of ZnO and help build ZnO based optical waveguide structures.

These interesting materials have been prepared by the sol-gel process [16], spray pyrolysis [17-19], pulsed-laser deposition [20], molecular beam epitaxy [21], DC reactive magnetron sputtering [22], co-evaporation [23], and plasma-enhanced metal organic chemical vapor deposition [24]. Conspicuously absent from this array of preparation techniques are electrodeposition and combustion synthesis.

1.4 Electrodeposition

An electrodeposition can be defined as the deposition of a substance on an electrode by the action of electricity (an electric current is applied between two electrodes separated by an electrolyte). The reaction essentially takes place at the electrode-electrolyte interface known as the electrical double layer. The electrochemical system, on the whole, is heterogeneous since the distribution of electrons and reactant species in the bulk and at the interfaces differ significantly.

A simple electrodeposition system consists of the following components:

Electrolyte: The electrolyte or bath provides the ions to be deposited. It could be aqueous, non-aqueous or molten. It should be electrically conductive and must contain the appropriate precursors e.g., metal salts, monomers etc.

Electrodes: The electric field, which provides the main driving force for the deposition, is applied between two electrodes, the anode (oxidizing electrode) and the cathode (reducing electrode). Cathodic deposition is generally more popular when depositing metals or metal oxides since (a) most metal ions are positive

ions and (b) anodic deposition often produces films with poor stoichiometry and adhesion. A third 'reference' electrode is used especially during potentiostatic depositions (see below) to maintain potential control.

Power supply: The power supply could be (a) a direct current at constant voltage, which leads to potentiostatic electrodeposition, (b) a direct constant current, which leads to galvanostatic electrodeposition or (c) a current or voltage waveform or pulse [25].

Electrochemical techniques offer a number of advantages over chemical routes some of which are stated below:

-electrochemical reactions are often much cleaner, with respect to possible pollutants, than chemical reactions

-economical considerations often favor the electrochemical route over existing chemical processes

-there are a number of examples where electrochemical routes produce unique products and do so in reaction pathways which themselves are unique

-electrochemical routes can be controlled exceptionally well by means of electrode potentials and electrode materials, to give a high selectivity of the desired product

-the same reactor can sometimes be used to produce useful products at both the cathode and the anode [26]

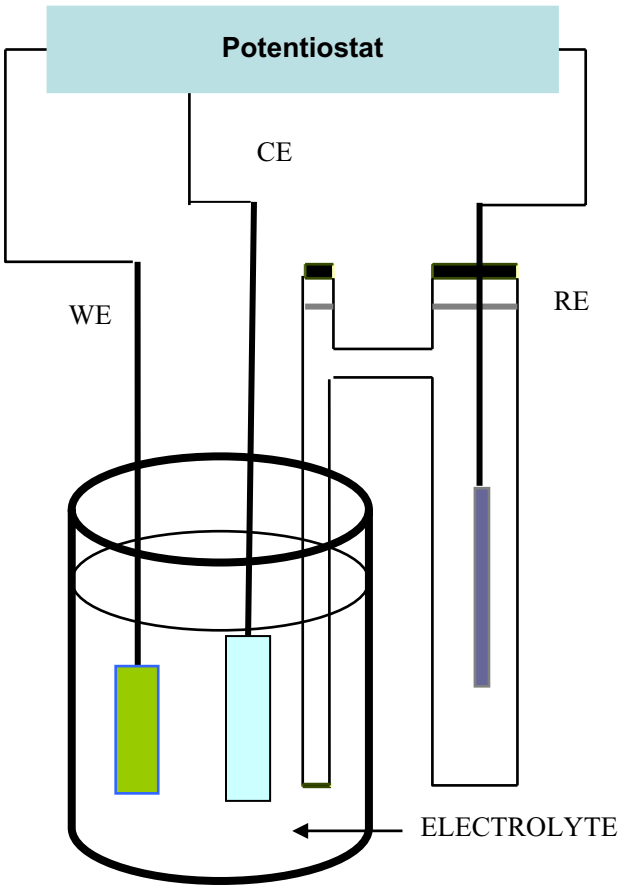

Figure 1.3 Standard setup for potentiostatic electrodeposition.

1.4.1. Semiconductor Electrodeposition

Electrodeposition of single elements, especially metals, is a well-established technique that has been used for decades in the extraction of metals from their ores and in the coating of jewelry with noble metals such as gold and silver. However, the use of this method for the growth of semiconducting materials is relatively new, having been first introduced in the late 1970s. In the subsequent years, electrodeposition of II-VI semiconductors led to the fabrication of solar cells with remarkable efficiencies and thus stimulated worldwide interest in the field. The work has now spread into many other materials including III-V, I-III-VI_2, and other alloy semiconductors. There have also been attempts to grow elemental semiconductors such as silicon [27] and mechanically harder

materials such as nitrides [28]. A few of the advantages of the method with regard to semiconductors include its simplicity and scalability, the ability to obtain intrinsically and extrinsically doped materials and the ability to engineer the band gap of the deposited semiconductors [29].

A brief review of the method as applicable to ZnO will now be presented.

Cathodic electrodeposition of ZnO

The cathodic electrodeposition of ZnO involves the generation of hydroxide ions at the surface of an electrode (cathode) by the reduction of an oxygen precursor. The three most commonly used oxygen precursors for this purpose include nitrate ions, dissolved molecular oxygen and hydrogen peroxide. The reaction schemes for the electrogeneration are illustrated below:

$$NO_3^- + H_2O + 2e^- \rightarrow NO_2^- + 2OH^- \quad (1.1)$$

$$\tfrac{1}{2}O_2 + H_2O + 2e^- \rightarrow 2OH^- \quad (1.2)$$

$$H_2O_2 + 2e^- \rightarrow 2OH^- \quad (1.3)$$

The process leads to an increase in pH in the vicinity of the electrode and to a local supersaturation for ZnO precipitation which provokes the formation of a zinc oxide film on the electrode surface [30].

ZnO films with a remarkable structural quality (high resolution transmission electron microscopy (HRTEM) results have shown that the electrodeposited grains are generally free of extended defects and stacking faults) can be prepared by this method, with different morphologies ranging from arrays of single crystal microcolumns to continuous films depending on the solution composition, deposition time and substrate activation.

Doping of ZnO films with a variety of elements has been successfully accomplished by electrodeposition. Examples include Al and In doping, which have been achieved by the addition of their respective chlorides into the deposition baths, and boron doping which has been achieved by using dimethylamineborane [31].

1.5 Combustion synthesis

Combustion synthesis also known as self-propagating high-temperature synthesis (SHS) or furnaceless synthesis is a technique that makes use of highly exothermic redox chemical reactions between metals and non-metals, the metathetical reaction between reactive compounds or reactions involving redox compounds/mixtures. The term 'combustion' covers flaming (gas-phase), smoldering (heterogeneous) as well as explosive reactions. The combustion method has been successfully used in the preparation of a number of technologically useful oxides (refractory oxides, semoconductors, dielectrics, magnetic materials, insulators, catalysts, phosphors, sensors etc.) and non oxides (carbides, borides, silicides, nitrides etc.) [32]. The method has a number of advantages over conventional fabrication methods, namely:

- simple and inexpensive
- high yields
- good ability to achieve high purity crystalline materials
- ability to synthesize multiphase complex oxide powders

Two of the most popular combustion methods for generating inorganic compounds, especially simple/complex oxides are:

Combustion synthesis using redox compounds

This approach involves the use of combustible precursors that can be ignited at low temperatures (<500^{o}C) to initiate gas-producing exothermic reactions which is self propagating and yield voluminous particle oxides. Compounds like $(NH_4)_2Cr_2O_7$ which contain both oxidizing ($Cr_2O_7^-$) and reducing (NH_4^+) groups when properly ignited ($KClO_3$-sucrose-H_2SO_4) decompose autocatalytically to yield voluminous Cr_2O_3 :

$$(NH_4)_2Cr_2O_7\ (s) \rightarrow Cr_2O_3\ (s) + N_2\ (g) + 4H_2O\ (g) \qquad (1.4)$$

The exothermicity of the combustion reaction is due to the oxidation of (NH_4^+) to N_2 and H_2O by the dichromate ion which itself is reduced to Cr^{3+}. The combustion is of a smoldering type and is accompanied by the evolution of gases resulting in a fine, voluminous powder.

A number of simple and mixed oxides such as spinel chromites, ferrites and cobaltites have been prepared by this method using precursors such as $(NH_4)_2M(CrO_4)_2.6H_2O$ (M=Mg, Ni) and $MFe_2(C_2O_4)_3(N_2H_4)_x$ (x=5 when M=Mg and x=6 when M=Mn,Co,Ni,Zn). While the method is simple and attractive, there are however, a number of limitations. Firstly, the exothermicity of the precursors is often not high enough to sustain combustion and an external heat source is required for the completion of the decomposition. Secondly, the preparation of the precursors is cumbersome and requires several days. Lastly, the yields are often low (~20% of the precursor).

Solution Combustion synthesis using redox mixtures

This approach involves the heating and evaporation of an aqueous metal nitrate solution with an organic compound (such as glycine, urea, citric acid etc.) resulting in a

self-sustainable reaction. The exothermicity of the reaction guarantees the attainment of high temperatures thus resulting in the formation of crystalline unagglomerated oxide powders in a short period of time. This method also offers the advantage of high chemical homogeneity since the initial reagents are mixed in the form of an aqueous solution and, as a result, favors the production of phases or ceramic compositions with multicomponents [33]. A wide range of materials have been prepared via this route including catalysts, ceramics, perovskites, and binary oxides such as SnO_2 and TiO_2.

1.5.1. Combustion Synthesis of ZnO

The first reports on the preparation of ZnO by combustion synthesis appeared in 1998 [33]. The synthesis technique involves the rapid heating of a saturated aqueous solution containing zinc nitrate and a reagent reducer (fuel) to a point at which combustion occurs.

Stoichiometric compositions of the combustion mixtures are calculated based on principles used in propellant chemistry [43]. The total oxidizing and reducing valencies of the oxidizer (O) (in this case zinc nitrate) and fuel (F) (in this case urea) serve as numerical coefficients for the stoichiometric balance and help us calculate the equivalence ratio ($\Phi c = O/F$). For this purpose, the elements C, H and Zn are considered as reducing elements with corresponding valencies +4, +1, and +2. The valency of N is considered 0. Oxygen is taken to be an oxidizing element with valency -2. (i.e., the oxygen content of zinc nitrate is exactly sufficient to completely consume/oxidize the fuel).

The adiabatic flame temperature (T_{ad}) of the reaction, which can be calculated using the following equations:

$$Q = -\Delta H^\circ = \int_{298}^{Tad} \left(\sum n \cdot c_p\right)_{products} dT \quad (1.5)$$

$$\Delta H^\circ = \left(\sum n \cdot \Delta H_f^\circ\right)_{products} - \left(\sum n \cdot \Delta H_f^\circ\right)_{reactants} \quad (1.6)$$

(n is the number of moles, ΔH^o is the enthalpy of the reaction, c_p is the heat capacity of the products at constant pressure, Q is the heat absorbed by the products under adiabatic conditions and ΔH_f^o is the standard enthalpy of formation) is a monotonically decreasing function of the equivalence ratio (Φc).

However, studies have shown that the measured values of the combustion temperatures (T_c) are typically lower than the calculated adiabatic flame temperature (T_{ad}) values due to heat losses. Also, T_c values tend to increase with decreasing Φc upto a point after which they tend to decrease. Combustion reactions involving fuel lean mixtures (Φc>>1) are generally slow, essentially flameless and result in powders with poor crystallinity. Reactions involving stoichiometric mixtures (Φc=1 i.e., the oxygen content of zinc nitrate is exactly sufficient to completely consume/oxidize the fuel) are relatively fast reactions that yield crystalline zinc oxide powders. When the precursor mixtures contain excess fuel, the combustion reactions need oxygen to be supplied externally. Since this process is limited by the diffusion rate, the combustion process tends to be relatively slower. However, the products obtained have been found to be crystalline, having a relatively small grain size [34].

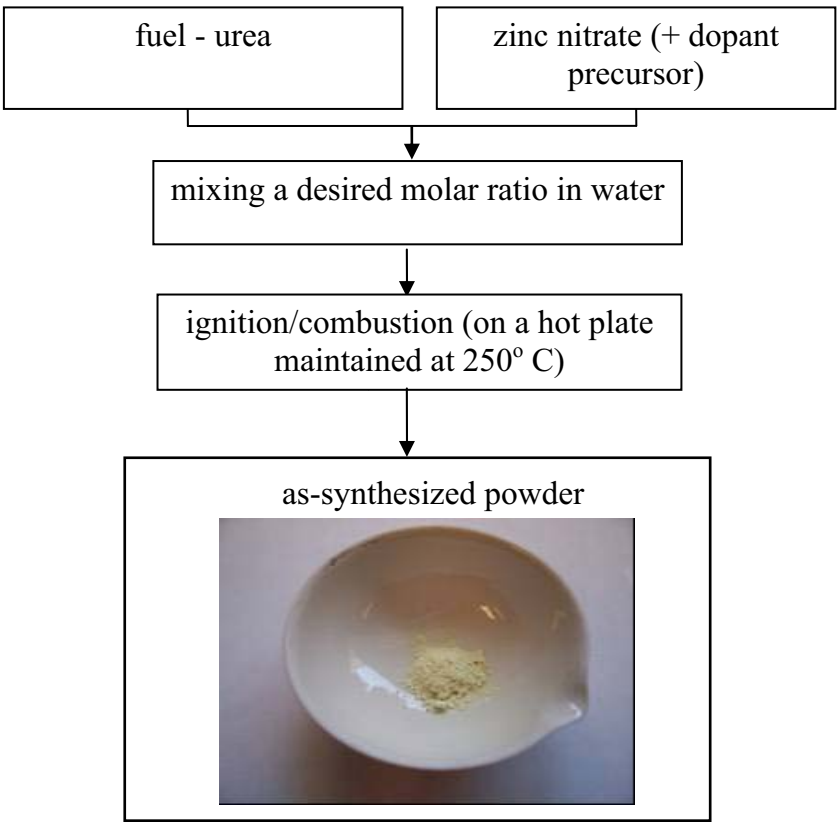

Figure 1.4 Flowchart for the combustion synthesis of ZnO powders.

Both doping and alloying of ZnO have been accomplished by this technique. Combustion synthesis of ZnO-Bi_2O_3 alloys for varistor applications [36], Li-doped ZnO nanocrystals for luminescence applications [35] and polytypes of $(ZnO)_mIn_2O_3$ [13] have been reported elsewhere.

1.6 Outline of the Thesis

In this thesis work, Cd-doped ZnO films were synthesized by cathodic electrodeposition from oxygenated KCl electrolyte containing $ZnCl_2$ and $CdCl_2$ in various molar ratios ranging from 0 mM to 5.0 mM each. The deposition mechanism was studied by cyclic voltammetry and studies were conducted on the films using X-ray

powder diffraction, diffuse reflectance, chronopotentiometry, X-ray photoelectron spectroscopy, and photoaction spectroscopy.

Cadmium- and Indium-doped ZnO were prepared by combustion synthesis using $CdCl_2$ and $InCl_3$ as dopant precursors along with zinc nitrate and urea as the combustion mixture. The doped samples were compared and contrasted with undoped ZnO using scanning electron microscopy, X-ray powder diffraction, energy-dispersive X-ray analyses, X-ray photoelectron spectroscopy, diffuse reflectance spectroscopy, and photoaction spectroscopy.

CHAPTER 2

EXPERIMENTAL

Transparent conducting oxide (TCO) substrates for the electrodeposition of Cd-doped zinc oxide substrates consisted of F-doped tin oxide (Nippon Sheet Glass Ltd.) coated on soda-lime glass. They were nominally ca. 400 nm thick and had a sheet resistance of 10.3 Ω/□. Strips (0.70 cm x 2 cm) were cut and cleaned in three 5 min steps of cleansing by ultrasonication in acetone, ethanol and finally ultrapure water. All solutions in this study were prepared from double-distilled (Corning Megapure) water. The thin films were cathodically electrodeposited from baths containing different molar ratios (Table 2.1) of $ZnCl_2$ and $CdCl_2$ in 0.1 M KCl as supporting electrolyte. The process was carried out by potentiostatic deposition at -0.725 V for 30 minutes. The deposition bath temperature was maintained at 70 ^{0}C. All electrodeposition baths were sparged with ultrapure O_2 for 30 min prior to use and an O_2 overpressure was maintained during film deposition. In some instances, N_2-saturated media were also used. After deposition, the oxide films were then subjected to a post-deposition thermal anneal at 450 ^{0}C for 1 h in air using a Model 650-14 Isotemp Programmable Muffle Furnace (Fisher Scientific). A linear heat ramp (at 10 ^{0}C/min) from room temperature to a pre-selected final temperature of 450 ^{0}C was followed by a 1 h equilibration at the final temperature. The samples were then allowed to cool via natural convection on the furnace back to the ambient condition.

Table 2.1 Electrodeposition bath compositions.

Sample no	$ZnCl_2$ concentration in bath, mM	$CdCl_2$ concentration in bath, mM
1	5.0	0.0
2	4.8	0.2
3	4.5	0.5
4	4.0	1.0
5	3.2	1.8
6	2.5	2.5
7	0.0	5.0

For the combustion synthesis of Cd-doped, In-doped and undoped ZnO chemicals were obtained from commercial sources and were the highest purity available. Zinc nitrate (Alpha Aesar, 99%), urea (J. T. Baker, 99.995%), indium chloride (Alfa Aesar, 99%), and cadmium chloride (Merck, 99%) were used without further purification. Urea was used as the fuel (reducing agent). Stoichiometric compositions of the combustion mixtures were calculated based on the total oxidizing and reducing valencies of the oxidizer (O) and fuel (F) (in this case urea) so that the equivalence ratio ($\Phi c = O/F$) was unity [43]. The combustion mixtures thus formulated, contained zinc nitrate and urea in the mole ratio 1:1.667. $CdCl_2$ (for Cd-doped ZnO) and $InCl_3$ (for In-doped ZnO) were added such that the atom ratios [Cd]/([Cd]+[Zn]) and [In]/([In]+[Zn]), in the combustion mixtures were both equal to 0.06.

Aqueous solutions of the combustion mixtures were poured into a platinum crucible and placed on a hot plate that was preheated to a nominal temperature of 250 ^{o}C. The solutions initially melted and underwent dehydration followed by decomposition which was accompanied by the release of a large amount of gases (oxides of nitrogen, NH_3 and HCNO). The mixtures then took on a viscous appearance and rapidly generated a mild explosion producing a dry foamy oxide as the product.

For photoaction spectroscopy measurements, the powders were thoroughly washed with double-distilled (Corning Megapure) water and coated onto the TCO substrates. These substrates consisted of Sn-doped indium oxide (ITO) coated on soda-lime glass. They were nominally ca. 60-100 nm thick and had a sheet resistance of 15-25 Ω/□. Substrate strips (0.70 cm x 2 cm) were cut and cleaned in three 5 min steps of cleansing by ultrasonication in acetone, ethanol and finally ultrapure water. Doped and undoped ZnO films were then made by dip-coating the TCO substrates in the powder suspensions (2-propanol containing 10 g/L oxide dose) after carefully masking one side with cellophane tape. After the dip, the films were baked in the oven for 10 min at 300 °C. The dip-bake sequence was repeated eight times, after which the final coated films were baked for 17 h at 300 °C. The oxide film thus built up on the ITO surface had a thickness in the 0.5-1.0 μm range.

A standard single-compartment, three-electrode cell was used in all the electrochemical experiments. A Pt coil and a Ag|AgCl|satd. KCl probe (Microelectrode Inc.) served as the counter- and reference electrodes respectively. All potentials below are quoted with respect to the Ag/AgCl reference. The electrodeposition experiments were carried out on a 100A Electrochemical Analyzer [Bioanalytical Systems (BAS), W.

Lafayette, IN]. Photoaction spectroscopy was performed on a Model CV-27 BAS Voltammograph equipped with a Model VP-6414S Soltec X-Y recorder. The monochromator used was a Thermo Jarrel Ash Corporation Model 82-415 with a grating blazed at 300 nm. The light source was a 150 W xenon arc lamp (Oriel, Stratford, CT) with an output of ~4.1 mW/cm^2, as measured with an Oriel Model 70260 Radiant Power/Energy meter. For linear sweep photovoltammetry experiments, the full output of a 75 W xenon arc lamp (Oriel, Stratford, CT) was used with the radiation being interrupted using a custom-built light chopper. The chronopotentiometry experiments, where the open-circuit potential of the oxide film was monitored as a function of time, also utilized the above electrochemical instrumentation.

X-ray photoelectron spectroscopy (XPS) used a Perkin Elmer/Physical Electronics Model 5000C system. Diffuse reflectance spectroscopy was performed on a Perkin-Elmer Lambda 6 spectrophotometer with $BaSO_4$ as the standard. Films were cast on glass slides (25 mm x 25 mm) for this purpose. X-ray powder diffraction (XRD) patterns of the samples were obtained on a Siemens D-500 powder diffractometer using Cu Kα radiation. The step size and the dwell time were set to 0.01 degree and 1 second respectively in order to obtain high resolution diffractograms. Scanning electron microscopy (SEM) images and energy dispersive X-ray (EDX) analyses were obtained using a Zeiss Supra 55 instrument with nominal electron beam voltages of 5 kV and 10 kV respectively.

CHAPTER 3

RESULTS

3.1 Electrodeposition of Cd-doped ZnO

Cyclic Voltammetry

Figure 3.1 contains cyclic voltammograms for a TCO working electrode in 0.1 M KCl supporting electrolyte containing Zn^{2+} species (Fig. 3.1a) or a mixture of Zn^{2+} and Cd^{2+} species (Fig. 3.1b). The effect of O_2 saturation of the electrolyte medium is also brought about by these data which compare the voltammograms in N_2-saturated and O_2-saturated electrolytes. Control scans with N_2 purge and without Zn^{2+} or Cd^{2+} species were featureless with near zero current. In all the cases, the forward scan was initiated at 0 V.

Considering Figure 3.1a, in the presence of Zn^{2+} and N_2, a large cathodic current flow is obtained on the forward (negative-going) scan with onset around -1050 mV. On the return cycle (after switch at the -1200 mV limit), a large anodic current is seen. These two features are assigned to the deposition and stripping of zinc respectively on/from the TCO surface:

$$Zn^{2+} + 2e^{-} \rightarrow Zn \tag{3.1}$$

$$Zn \rightarrow Zn^{2+} + 2e^{-} \tag{3.2}$$

In the presence of dissolved O_2 in the electrolyte, a cathodic curve is observed with onset at -400 mV. This initial curve is assigned to the reduction of O_2 and the electrogeneration of base:

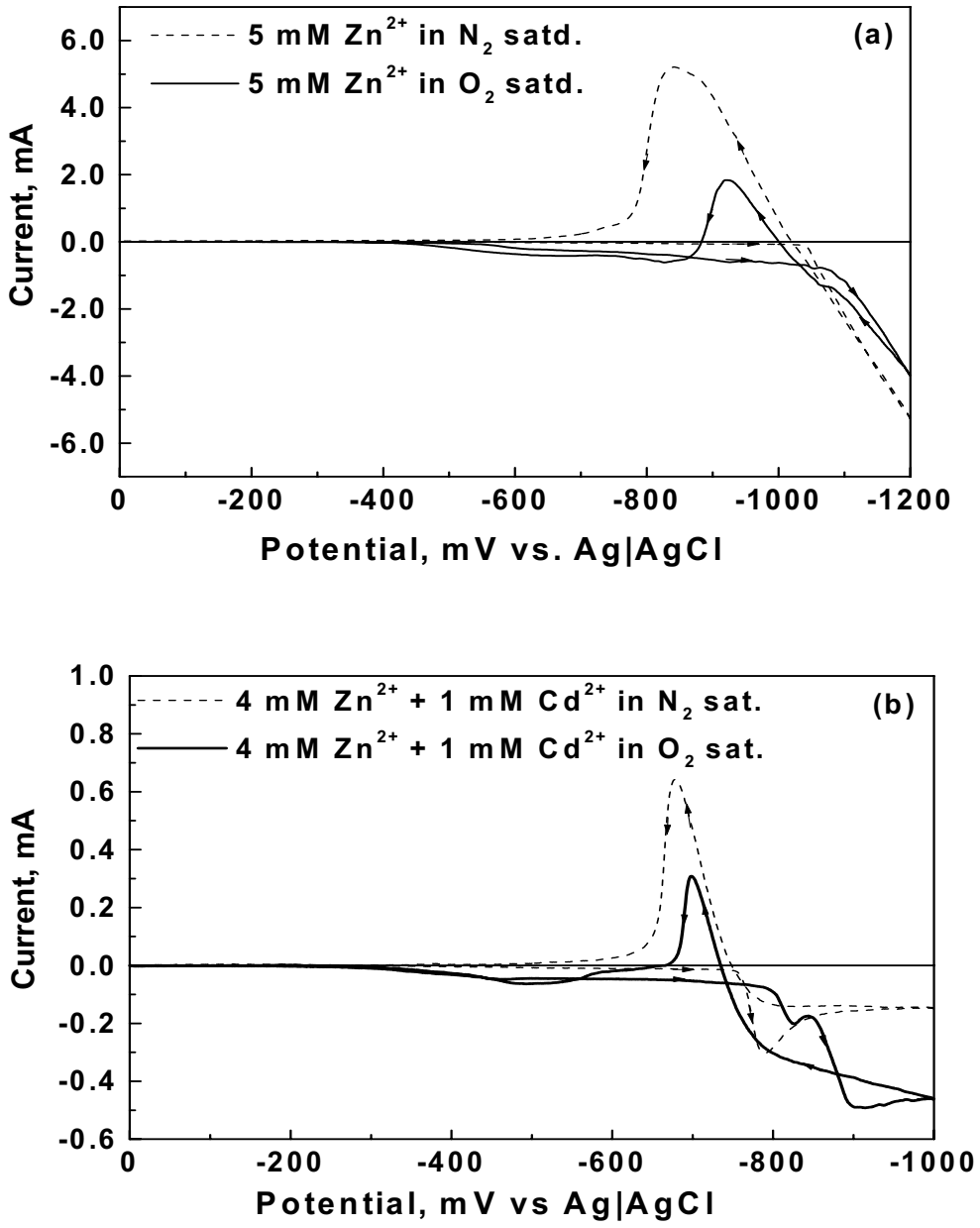

Figure 3.1 Cyclic voltammograms (potential scan rate 2 mV/s) for a TCO working electrode in 0.1 M KCl supporting electrolyte for (a) Zn-O and (b) Zn-Cd-O electrodeposition scenarios with solution compositions as shown (from Ref. 44).

$$\tfrac{1}{2}O_2 + H_2O + 2e^- \rightarrow 2OH^- \quad (3.3)$$

The deposition of Zn (as the oxide or hydroxide) (Reactions 3.4-3.6) occurs concomitantly and continues till -1100 mV, at which juncture, zinc metal is also deposited via Reaction 3.1. Note that the deposition potential for metallic zinc shifts to a more negative value in the presence of O_2 in the electrolyte. The reverse scan shows a much lower anodic current (relative to the N_2-saturated case) reflecting the fact that a lower amount of zinc metal is available to be anodically stripped.

$$Zn^{2+} + 2OH^- \rightarrow ZnO + H_2O \quad (3.4)$$

$$Zn^{2+} + \tfrac{1}{2}O_2 + 2e^- \rightarrow ZnO \quad (3.5)$$

$$Zn^{2+} + 2OH^- \rightarrow Zn(OH)_2 \quad (3.6)$$

Consider Fig. 3.1b when both Zn^{2+} and Cd^{2+} species are present in the KCl electrolyte. Interestingly, the voltammogram in the N_2-saturated case mimicks that seen with only Cd^{2+} in solution (not shown, see Ref. 37) and the features correspond to the cathodic deposition and anodic stripping of cadmium metal. The more relevant case pertains to O_2-saturated electrolyte and in this case, in addition to Reactions 3.3-3.6 considered above, Reactions 3.7-3.9 also occur:

$$Cd^{2+} + 2OH^- \rightarrow CdO + H_2O \quad (3.7)$$

$$Cd^{2+} + \tfrac{1}{2}O_2 + 2e^- \rightarrow CdO \quad (3.8)$$

$$Cd^{2+} + 2OH^- \rightarrow Cd(OH)_2 \quad (3.9)$$

Note that Reactions 3.5 and 3.8 can be considered as a summation of Reaction 3.3 and either Reaction 3.4 or Reaction 3.7 for the zinc and cadmium case respectively. Also, what is perhaps only subtly shown by the voltammetry data but is very clearly seen (even visually) in film depositions at fixed potentials is that the presence of Cd^{2+} enhances the deposition of ZnO on the TCO substrate surface.

All the films grown were nominally ~ 1 μm thick except for the CdO films which were ca. 3 μm thick. This is because the rate of CdO film growth is much higher than that of ZnO. In all the cases to be discussed below, the deposited films were subject to thermal anneal as described in the Experimental section. Interestingly, electron microscopy did not reveal significant changes in the film morphology before or after thermal anneal. However, the XRD patterns were much better defined for the samples after thermal anneal. Under these conditions, thermal anneal mainly serves to improve both the crystallinity and substrate contact quality of the electrosynthesized films. Further, any $Zn(OH)_2$ (Reaction 3.6) or $Cd(OH)_2$ (Reaction 3.9) that is deposited would be converted to ZnO and CdO respectively:

$$Zn(OH)_2 \xrightarrow{\Delta} ZnO + H_2O \quad (3.10)$$

$$Cd(OH)_2 \xrightarrow{\Delta} CdO + H_2O \qquad (3.11)$$

For all the cases below, the films were potentiostatically deposited at -0.725 V. Note that the deposition of Cd and Zn metal cannot occur at -0.725 V (see Figure 3.1b).

Scanning Electron Microscopy

Figure 3.2 contains a representative scanning electron micrograph of a doped oxide film; while the flake-like morphology characteristic of ZnO is clearly seen, the finer cauliflower-like grains characteristic of a phase separated CdO [37] are absent.

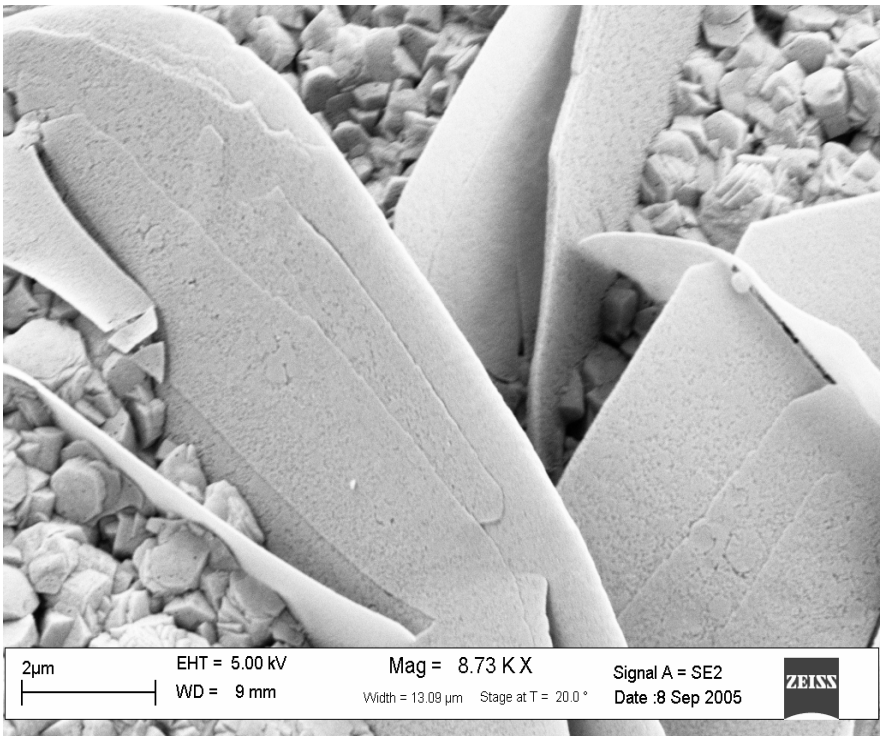

Figure 3.2 Representative SEM picture of a Cd-doped ZnO film electrodeposited at – 0.725 V from a bath containing 4 mM $ZnCl_2$ + 1 mM $CdCl_2$ (Sample 4).

X-Ray Diffraction

Figure 3.3 contains XRD patterns for five such doped samples, compared with the corresponding patterns for ZnO (Fig. 3.3a) and CdO (Fig. 3.3g) respectively. Note that none of the patterns in Figs. 3.3 b-f show any evidence for CdO. The diffraction peaks

are not shifted in the doped samples (relative to the undoped ZnO parent sample) presumably because of the rather low doping levels. Scherrer analyses of these XRD data using the equation:

$$D = \frac{0.89\lambda}{\beta \cos\theta} \text{ Å} \qquad (3.12)$$

where,

$\lambda -$ wavelength of copper Kα = 1.5405 Å

$\beta -$ full width at half maximum (in radians)

$\theta -$ diffraction angle

show variations in the grain size of the doped samples (Fig. 3.4).

Chronopotentiometric Analyses

Figure 3.5 shows the change in potential of two films in 0.5 M Na_2SO_4 supporting electrolyte to which an aliquot of Cu^{2+} species was added at a specific time (shown by arrows) in the figure. If any free Cd is present in the film an abrupt change in the potential would result from the galvanic reaction between Cu^{2+} and Cd, whereby the copper(II) species would be spontaneously reduced and Cd would be spontaneously oxidized to Cd^{2+} (the two relevant standard reduction potentials, Cu^{2+}/Cu and Cd^{2+}/Cd, are 0.539 V and -0.206 V respectively). Thus the top curve serves as a control; this particular CdO film was electrodeposited at -0.950 V and was not subjected to thermal anneal. Under these conditions, the CdO film would be admixed with free Cd (see Figure 3.1b) Indeed, when Cu^{2+} was added, the film (open-circuit) potential shows an immediate change diagnosing the occurrence of the spontaneous electron transfer process.

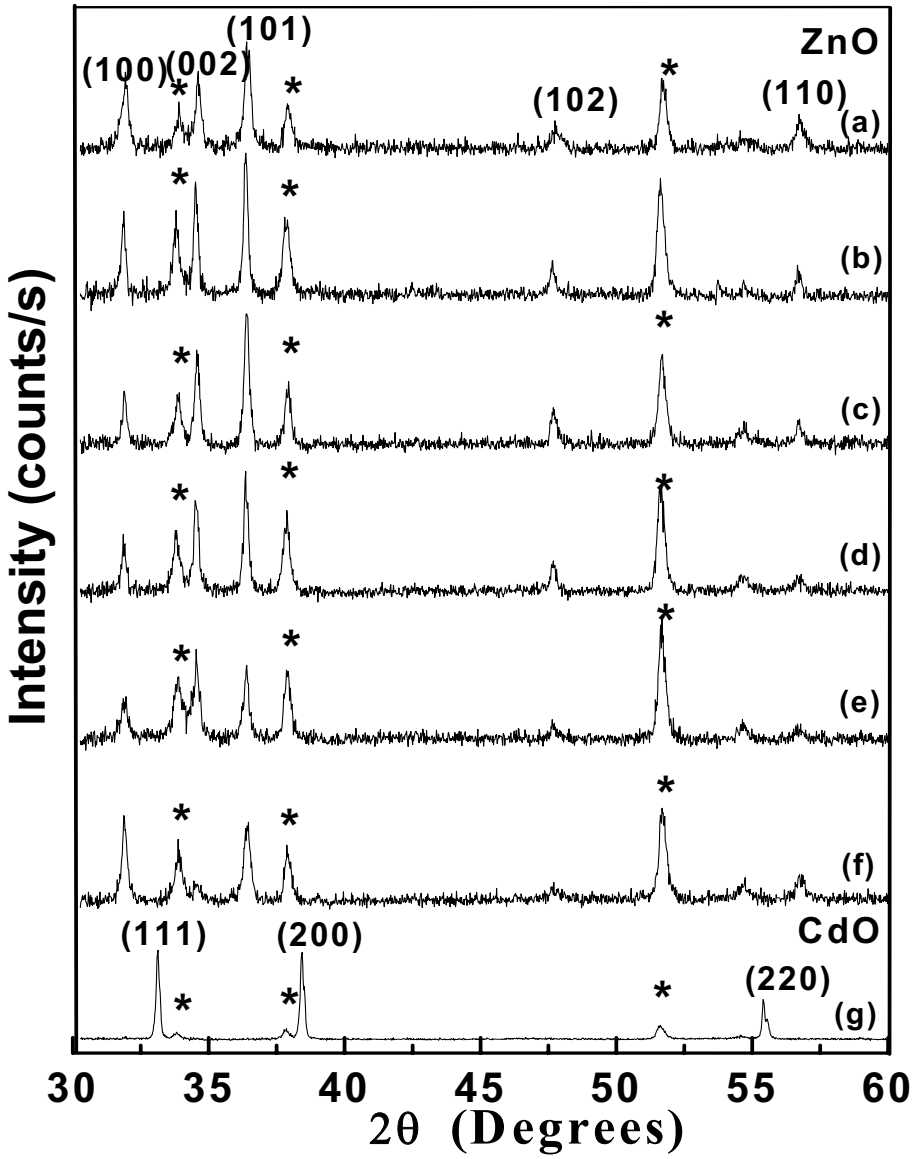

Figure 3.3 XRD patterns for the ZnO and CdO end-members (Figs. 3.3a and g) and five Cd-doped ZnO samples. (Refer Table 2.1) Fig. 3.3b: Sample 2, Fig. 5c: Sample 3, Fig. 5d: Sample 4, Fig. 5e: Sample 5, and Fig. 5f: Sample 6. The substrate peaks are indicated by asterisks.

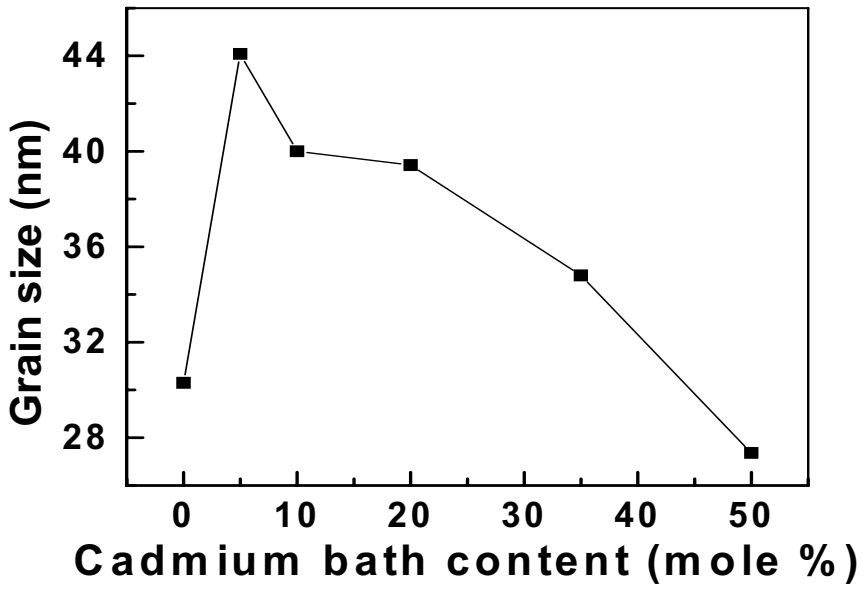

Figure 3.4 Plot of the grain size (as obtained from Scherrer analyses of the Cd doped ZnO peaks in the XRD data) versus Cd content of the electrodeposition bath.

On the other hand, a Cd-doped ZnO film shows no change in its open-circuit potential when Cu^{2+} species are dosed into the electrolyte showing the absence of free Cd in the doped ZnO sample. Thus the conclusion is inescapable from the absence of CdO (see Figure 3.3) and metallic Cd, that Cd is present in the film solely as a dopant.

Optical Behavior

Doping does alter the E_g value of the ZnO film as shown by the optical data in Figure 3.6. Figure 3.6 contains two representative Tauc plots of $(\alpha h\nu)^2$ vs $h\nu$ (α = optical absorption coefficient) constructed from diffuse reflectance data, whose intercepts correspond to 3.18 eV (for ZnO) and 3.03 (for the Cd-doped sample). Figure 3.7 shows the variation of E_g with the Cd-content of the doped ZnO film as expressed by the bath composition (see Table 2.1).

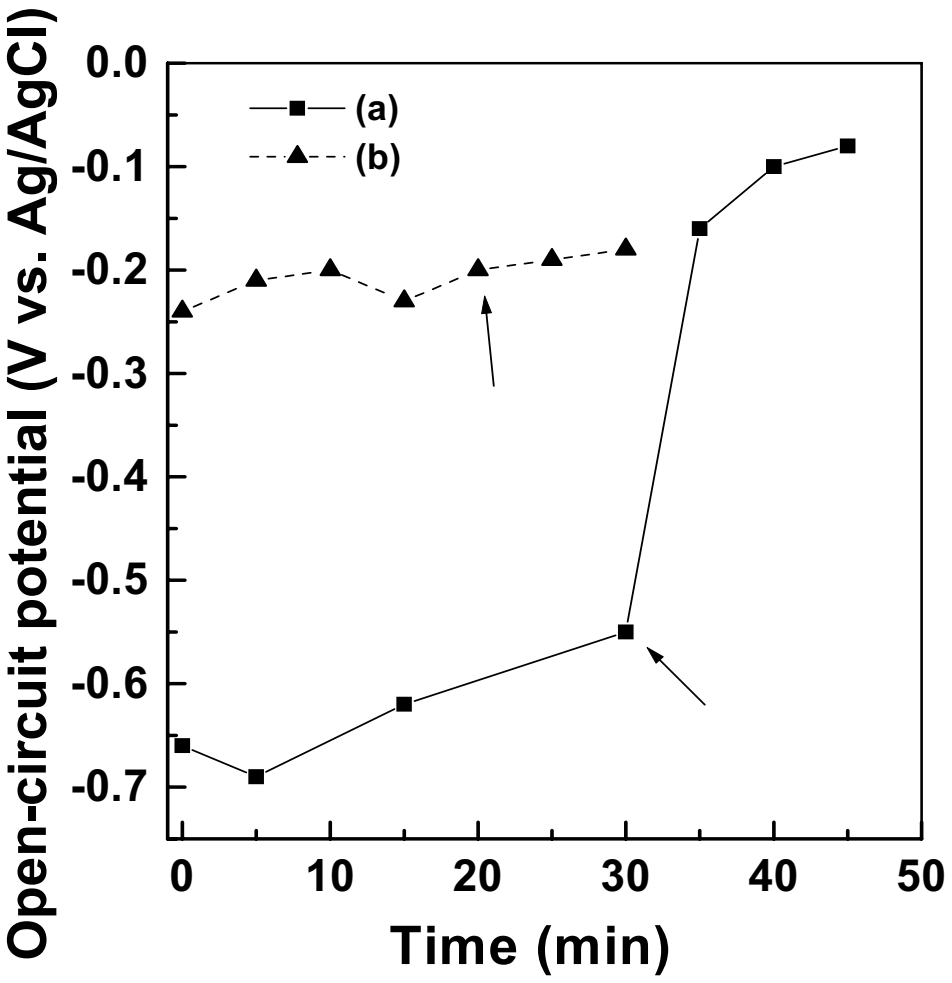

Figure 3.5 Chronopotentiometric data for (a) a pure CdO sample (not subjected to thermal anneal) and (b) a Cd-doped ZnO sample electrodeposited at –0.725 V from a bath containing 2.5 mM $ZnCl_2$ + 2.5 mM $CdCl_2$ (Sample 6) in 0.5 M Na_2SO_4 electrolyte. The arrows show when an aliquot of 5 mL of 0.1 M $CuSO_4$ + 0.5 M Na_2SO_4 was added to the electrolyte.

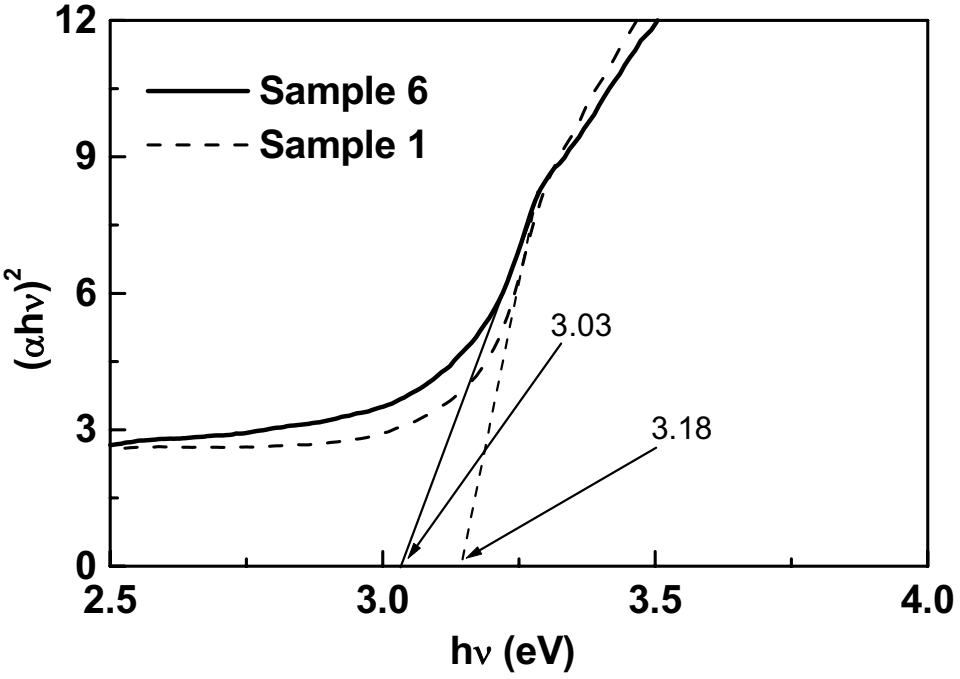

Figure 3.6 Tauc plots of $(\alpha h\nu)^2$ vs. $h\nu$ (constructed from optical transmittance data) for a Cd-doped ZnO sample electrodeposited at –0.725 V from a bath containing 2.5 mM $ZnCl_2$ + 2.5 mM $CdCl_2$ (Sample 6) compared with pure ZnO (Sample 1).

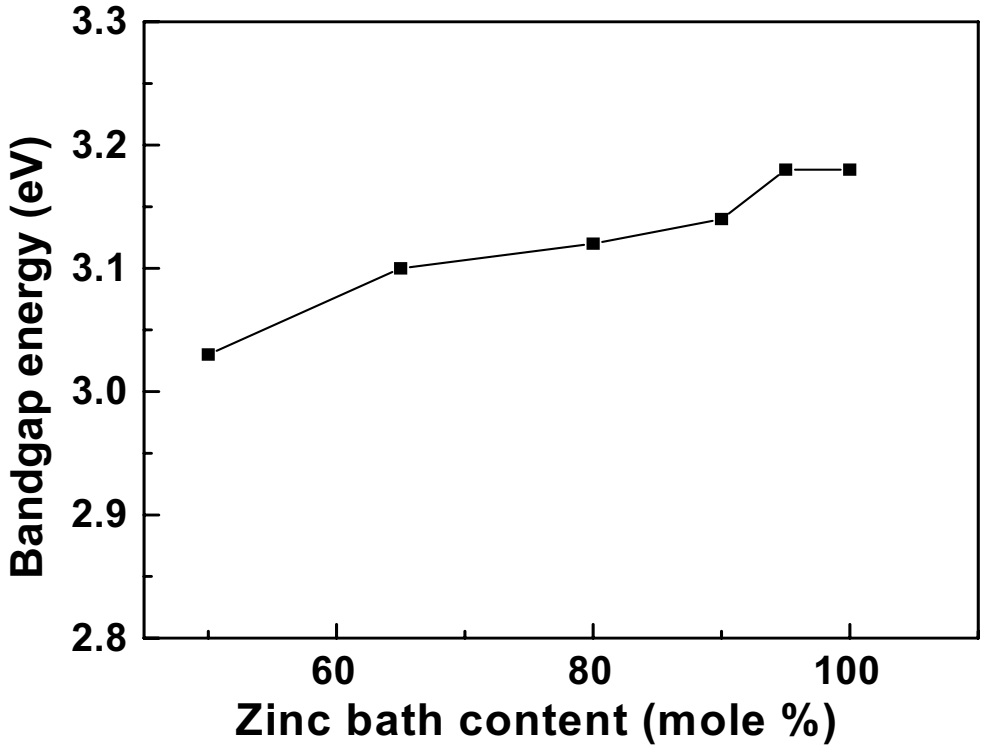

Figure 3.7 Plot of E_g of the Cd-doped ZnO samples as a function of the initial Zn content of the bath (The Zn bath content is expressed as: Zn/(Cd+Zn) mole%).

X-Ray Photoelectron Spectroscopy

The variation of (surface) Cd levels with the Cd-content of the electrolyte bath is shown by the XPS data in Fig. 3.8. A maximum surface (doping) level of Cd of 2.5 atom% was attained in this study from a 50:50 (Cd:Zn) electrolyte bath. High-resolution XPS data in the Cd binding energy region revealed the Cd $3d_{5/2}$ signal at 405 eV (Figure 3.9) is in very good agreement with the spectrum reported by previous authors for Cd-doped ZnO nanorods [38].

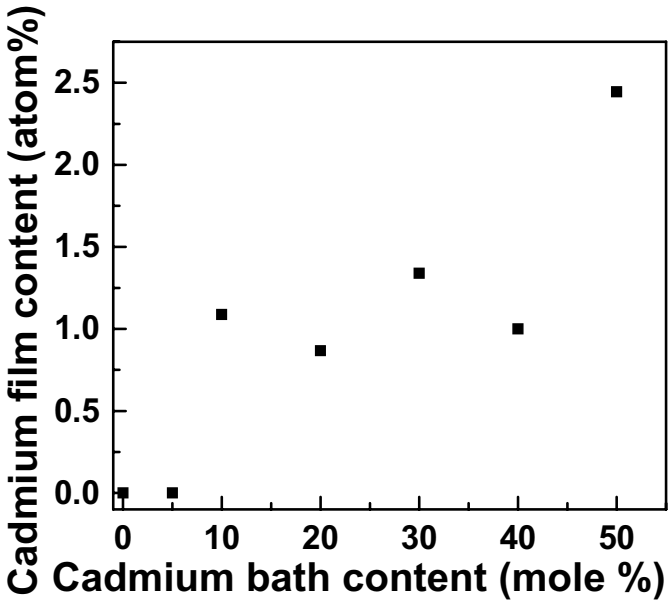

Figure 3.8 Plot of the XPS data on the Cd film content of the doped ZnO samples as function of the corresponding Cd content of the electrodeposition bath (the Cd film content is expressed as: Cd/(Cd+Zn) atom%. The Cd bath content is expressed as: Cd/(Cd+Zn) mole%).

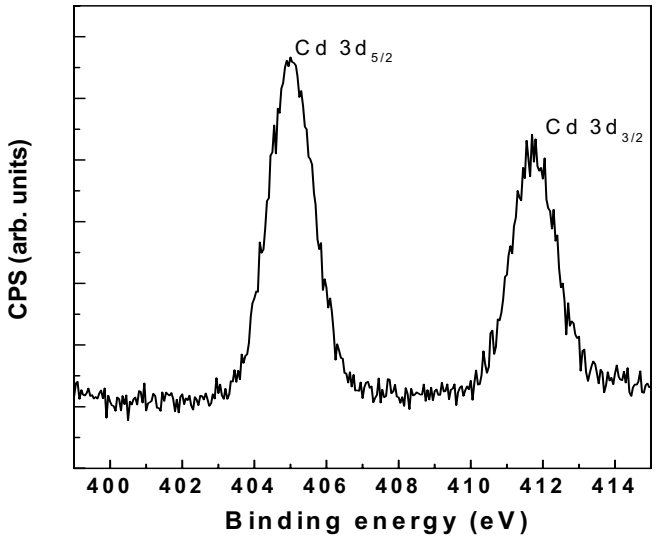

Figure 3.9 High resolution XPS spectrum in the Cd binding energy region for a Cd doped ZnO sample (Sample 6, Table 2.1).

Photoaction Spectra

Figure 3.10 contains photoaction spectra of the five Cd-doped ZnO samples compared with the spectrum for pure ZnO. The doped samples show a shift in the cut-off toward larger wavelengths (smaller E_g) consistent with the trend seen in Figure 3.7. Also importantly, the doped samples in general show higher incident photon-to-electron conversion efficiencies (IPCE).

Photovoltammetric Experiments

Finally, Fig. 3.11 contrasts linear sweep voltammograms under interrupted illumination (photovoltammetry) for doped and undoped ZnO samples. The potential of the oxide electrodes was slowly swept in these experiments in the positive direction in the reverse bias regime. The doped ZnO sample again shows a superior photoresponse. It is worth noting that both samples show good rectification behavior in the dark as diagnosed by the near absence of current flow without irradiation of the oxide surfaces. The anodic photocurrents in Figs. 3.10 and 3.11 presumably arise from the oxidation of electrolyte species (e.g., hydroxyl groups or water molecules) by the photogenerated holes in the oxide phase.

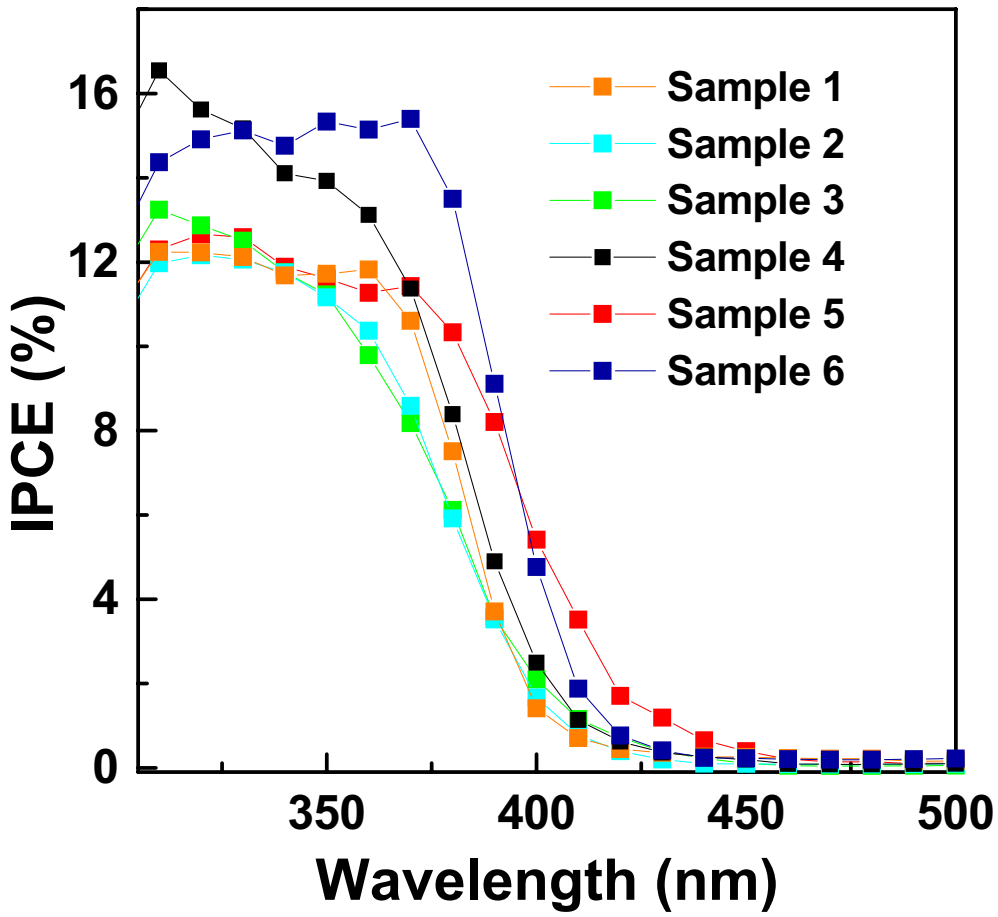

Figure 3.10 Photoaction spectra for pure ZnO (Sample 1) and five Cd-doped ZnO samples (Samples 2-6) in 0.5 M Na_2SO_4. The spectra were acquired at 0.31 V. IPCE stands for incident photon-to-electron conversion efficiency.

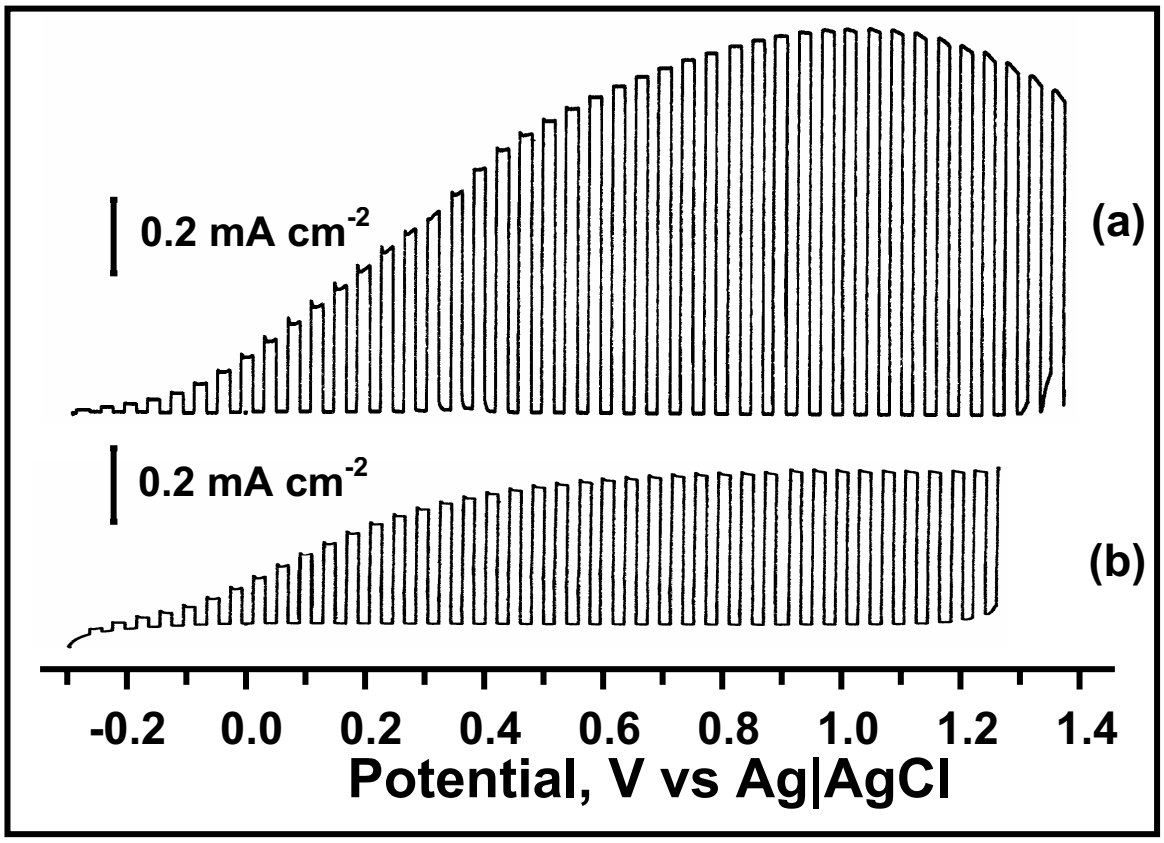

Figure 3.11 Photovoltammograms at 0.1 Hz chopped irradiation for (a) a Cd doped ZnO film electrodeposited at –0.725 V from a bath containing 4.5 mM $ZnCl_2$ + 0.5 mM $CdCl_2$ (Sample 3) (b) a ZnO film (Sample 1) in 0.5 M Na_2SO_4. Photovoltammograms were obtained at 2 mV s^{-1}; the full output of a 75 W xenon arc lamp was used in the experiment.

3.2 Combustion Synthesis of Cd-doped and In-doped ZnO

Preliminary observations

The use of cadmium nitrate as a dopant precursor in the combustion mixture did not result in Cd uptake by the zinc oxide matrix. This is because the nitrate salt generates the corresponding oxide during the combustion process. Interestingly, in the aforementioned study on the preparation of $(ZnO)_mIn_2O_3$ [13], precursor salts for both Zn and In were nitrate. On the other hand, for Li^+ doping of ZnO via the combustion method, the corresponding chloride salt was deployed [35]. Therefore, in all subsequent experiments on the Cd- and In-doped ZnO in the present study, $CdCl_2$ and $InCl_3$ were used as the dopant precursor respectively (see Experimental section). On the other hand, zinc nitrate was used as usual for generating ZnO during the combustion reaction.

Scanning electron microscopy

Figure 3.12 compares and contrasts the morphology of ZnO (Fig. 3.12a), Cd-doped ZnO (Fig. 3.12b), and In-doped ZnO (Fig. 3.12c) powders as obtained by combustion synthesis in this study. The doped samples are clearly finer-grained relative to the morphology of the undoped specimen. Interestingly, the Cd- and In-doped samples also present rather different morphologies for the ZnO grains (c.f., Figs. 3.12b and c).

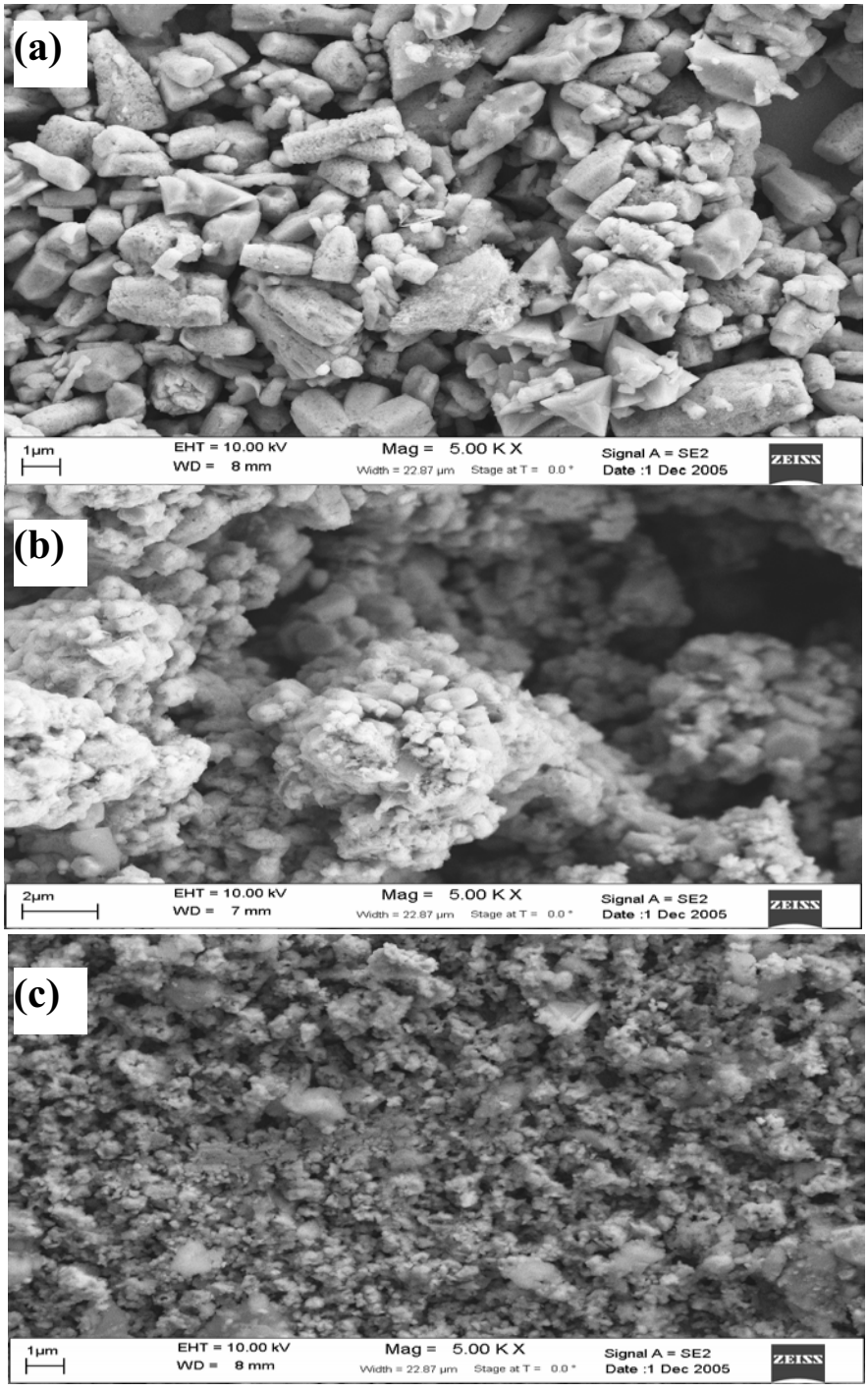

Figure 3.12 Representative SEM images of (a) undoped (b) Cd-doped and (c) In doped ZnO samples.

X- ray diffraction

Figure 3.13 compares and contrasts survey X-ray diffractograms for undoped ZnO, Cd-doped ZnO, and In-doped ZnO. No other reflections other than those corresponding to the host ZnO matrix are seen in these powder XRD patterns. It is worth noting that the as-prepared samples are highly crystalline in all the three cases attesting to the effectiveness of the combustion synthesis to induce in situ crystallization during oxide formation. By way of contrast, other preparation techniques (e.g., sol-gel chemistry, electrodeposition) usually require a post-deposition thermal anneal for inducing crystallinity in the prepared samples. The increased noise associated with the diffractograms of the doped samples is consistent with the smaller cluster size as seen by SEM.

The close correspondence of all the three XRD patterns in Fig. 3.13 (and assignable to ZnO) stands in stark contrast to the situation when $(ZnO)_mIn_2O_3$ is formed (distinct reflections assignable to $(ZnO)_3In_2O_3$ were observed when a gelled mixture of zinc and indium nitrates along with glycine was subjected to combustion [13]). Doping of the host ZnO matrix exerts a more subtle effect on the XRD behavior as illustrated in Fig. 3.14 for the Cd-doped and In-doped cases. The (100) reflection scan is amplified in this figure to show the influence of Cd and In incorporation into the ZnO lattice. Thus this peak is shifted from $2\theta = 31.84^0$ for the undoped ZnO case to 31.52^0 and 31.49^0 for the Cd-doped and In-doped cases respectively. These shifts of the diffraction peaks in the doped ZnO cases (relative to undoped ZnO) as well as the

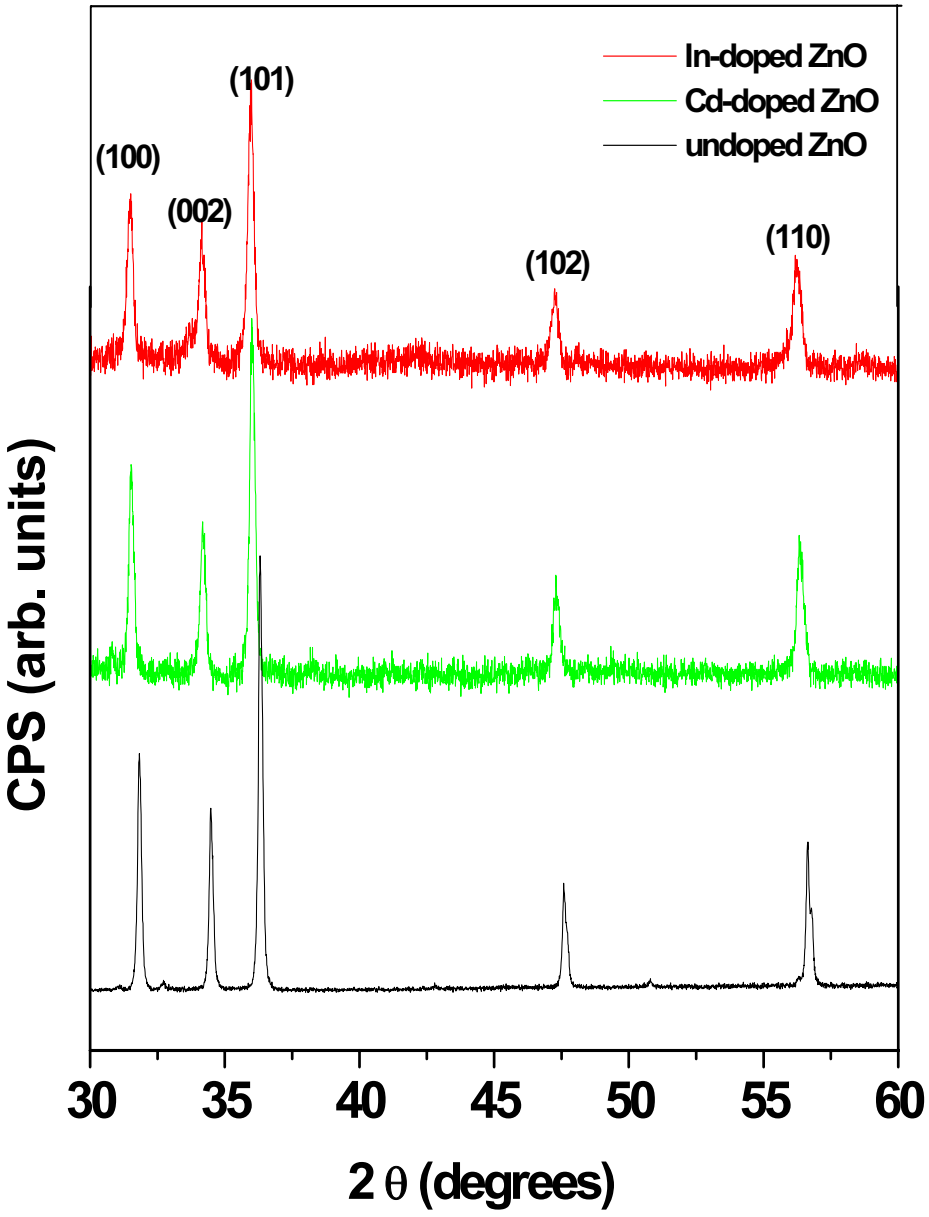

Figure 3.13 Comparison of survey XRD patterns for undoped, Cd-doped and In- doped ZnO samples.

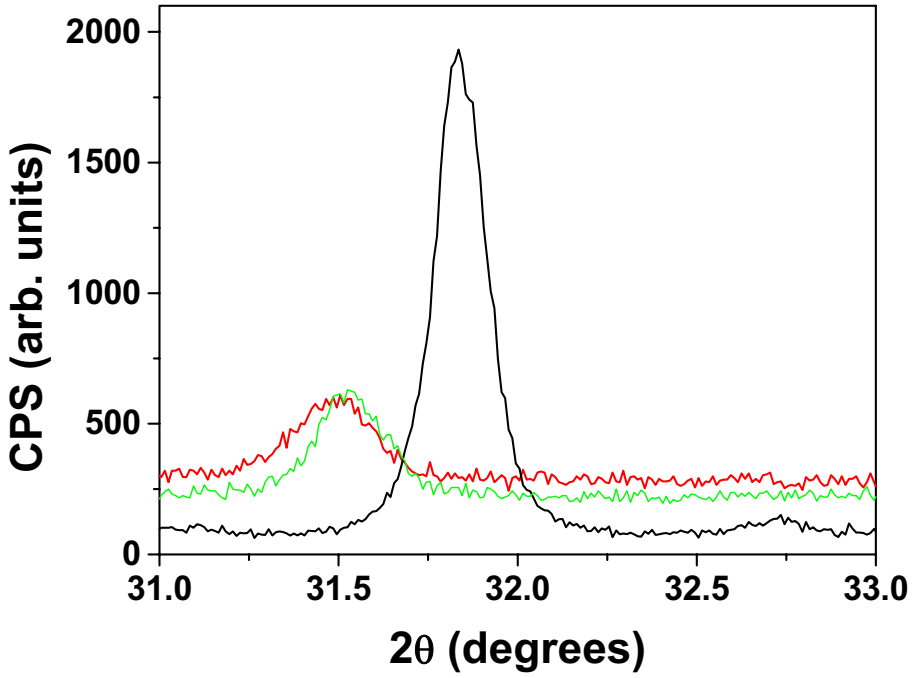

Figure 3.14 High-resolution diffractograms of the (100) peak for undoped, Cd- doped, and In-doped ZnO samples.

broadening induced from the ZnO lattice (the full width at half maximum (FWHM) of the (100) peaks in the undoped, Cd-doped, and In-doped ZnO samples, for example, are 0.16^0, 0.22^0 and 0.25^0 respectively), are both consistent with the strain induced by dopant incorporation.

The lattice unit cell constants a and c for the undoped, Cd-doped and In-doped ZnO samples were estimated based on the positions of the (100) and (002) peaks using the equation:

$$d_{(hkl)} = \frac{a}{\sqrt{\frac{4}{3}(h^2 + k^2 + hk) + \frac{l^2 a^2}{c^2}}} \quad [19] \qquad (3.13)$$

and were found to be a = 3.240 Å, c = 5.195 Å, a = 3.274 Å, c = 5.237 Å, and a = 3.277 Å, c = 5.243 Å respectively. The increase in the unit cell dimensions for the doped samples (relative to the starting material) is consistent with the notion of induced strain by the dopant.

The FWHM of the XRD peaks can be expressed as a linear combination of the contribution from lattice strain and crystal size using the equation:

$$\frac{\beta \cos \theta}{\lambda} = \frac{1}{\varepsilon} + \frac{\eta \sin \theta}{\lambda} \tag{3.14}$$

where β is the measured FWHM, θ is the Bragg angle of the peak, λ is the X-ray diffraction wavelength, ε is the effective particle size, and η is the effective strain. β cos θ/λ was plotted versus sin θ/λ for the samples (Figure 3.15) and the effective particle sizes for the undoped, Cd-doped and In-doped samples (taking strain into account) were found to be equal to 99.0 nm, 60.1 nm and 73.4 nm respectively.

Energy-dispersive X-ray (EDX) analyses

Figure 3.16 contains the EDX spectra for undoped (Fig. 3.16a), Cd-doped (Fig. 3.16b), and In-doped ZnO (Fig. 3.16c) samples. Quantitative analyses of these data afford Cd and In atom ratios of 0.106 and 0.0992 respectively in the ZnO host matrix. The Cl signals in the EDX spectra of the doped samples (Figs. 3.16b and c) originate from the corresponding chloride precursors used.

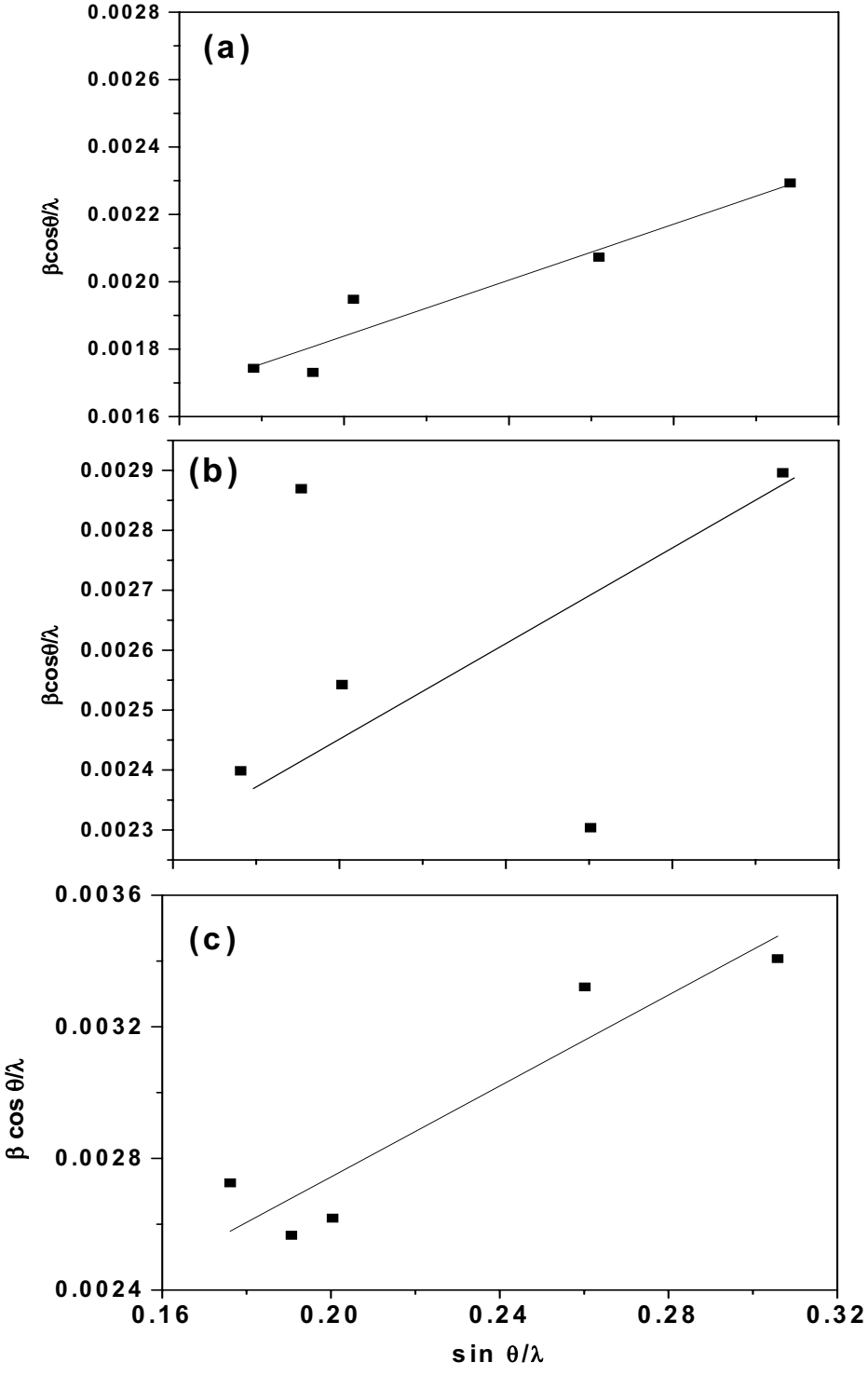

Figure 3.15 βcosθ/λ vs sinθ/λ plotted using X-ray diffraction data for (a) undoped (b) Cd-doped and (c) In-doped ZnO.

X-ray photoelectron spectroscopy

Figures 3.17a and b contain survey XPS data for Cd- and In-doped ZnO samples respectively. In the high-resolution spectra (not shown), the dopant signals are split due to spin-orbit coupling into two peaks. Quantitative analyses of these data afford Cd and In atom ratios (relative to Zn) of 0.144 and 0.355 respectively.

Optical behavior

Figure 3.18 contains the UV-visible diffuse reflectance data for the undoped, Cd-doped, and In-doped ZnO samples in the 250-850 nm wavelength region. The transmittance is found to decrease with doping. This decrease may stem from the increased scattering of photons by either doping-induced crystal defects or due to the formation of grainy surfaces. The (increased) free carrier absorption of photons may also contribute to the reduction in optical transmittance.

The Tauc plots shown in Fig. 3.19 were constructed using the diffuse reflectance data in Fig. 3.18. The intercepts of these plots afford an estimate of the optical bandgap energy of the corresponding sample. A value of 3.14 eV is obtained for combustion-synthesized ZnO while the corresponding values for the doped samples are 3.07 eV (Cd) and 3.02 eV (In) respectively. Interestingly enough, the E_g value of the undoped ZnO samples is lower than that typical of ZnO obtained by other synthesis methods (3.2-3.3 eV). This is presumably because of the effect exerted by the carrier concentration in the host material as elaborated below. On the other hand, the E_g value is in accord with that previously reported for combustion-synthesized ZnO [35].

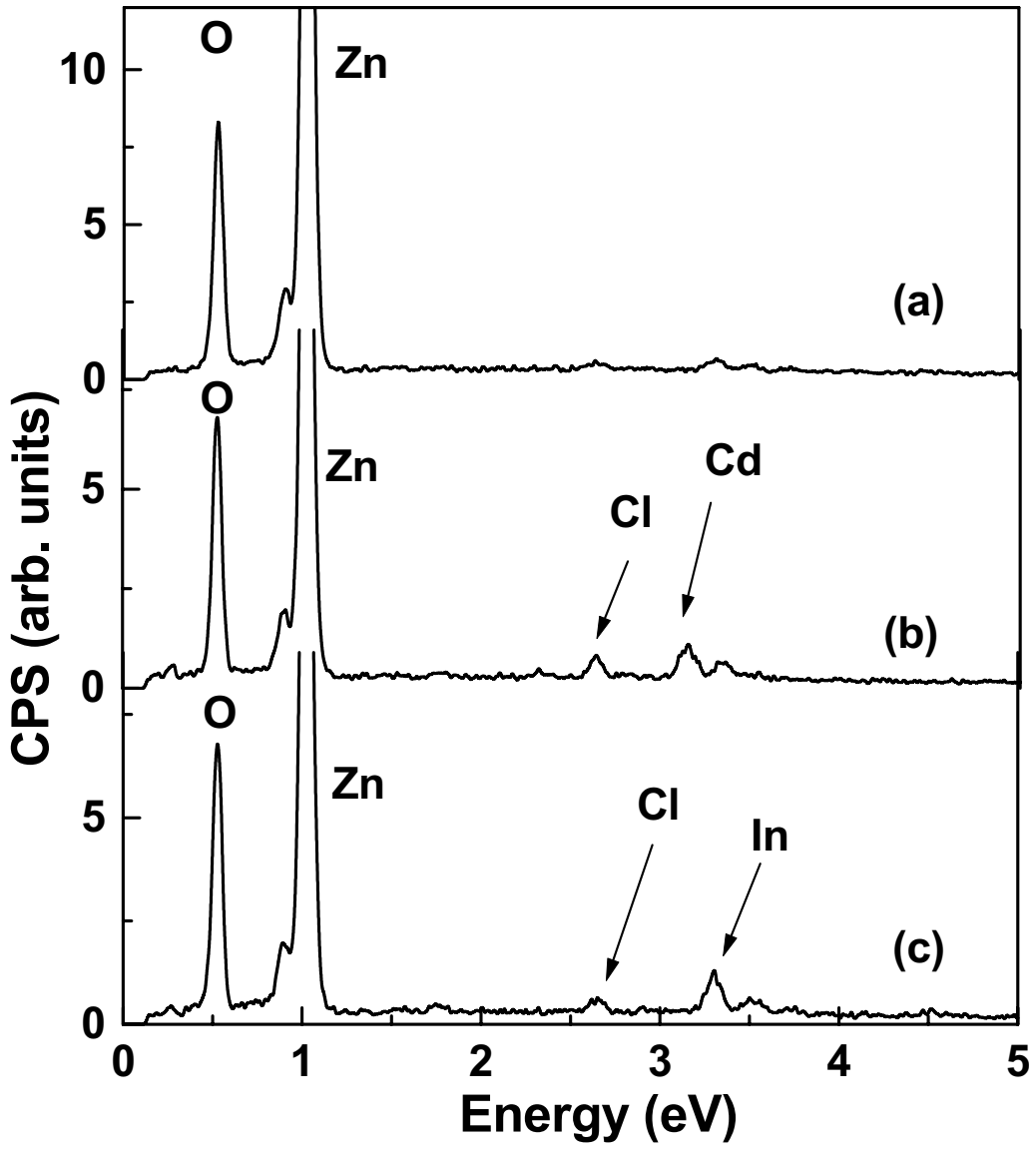

Figure 3.16 EDX spectra for (a) undoped (b) Cd-doped and (c) In-doped ZnO samples.

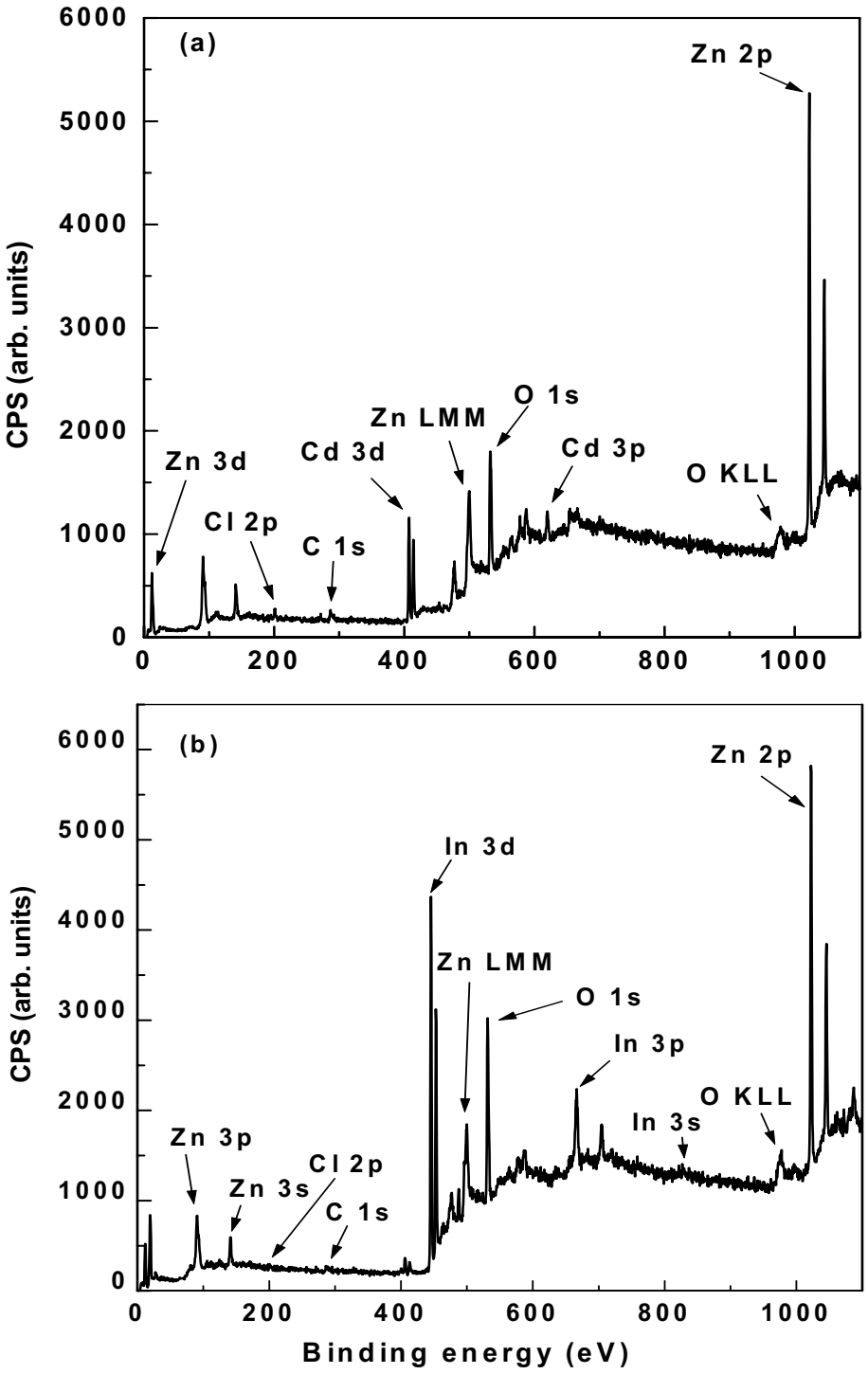

Figure 3.17 Survey XPS profiles for Cd-doped (Fig. 3.17a) and In-doped (Fig. 3.17b) ZnO samples.

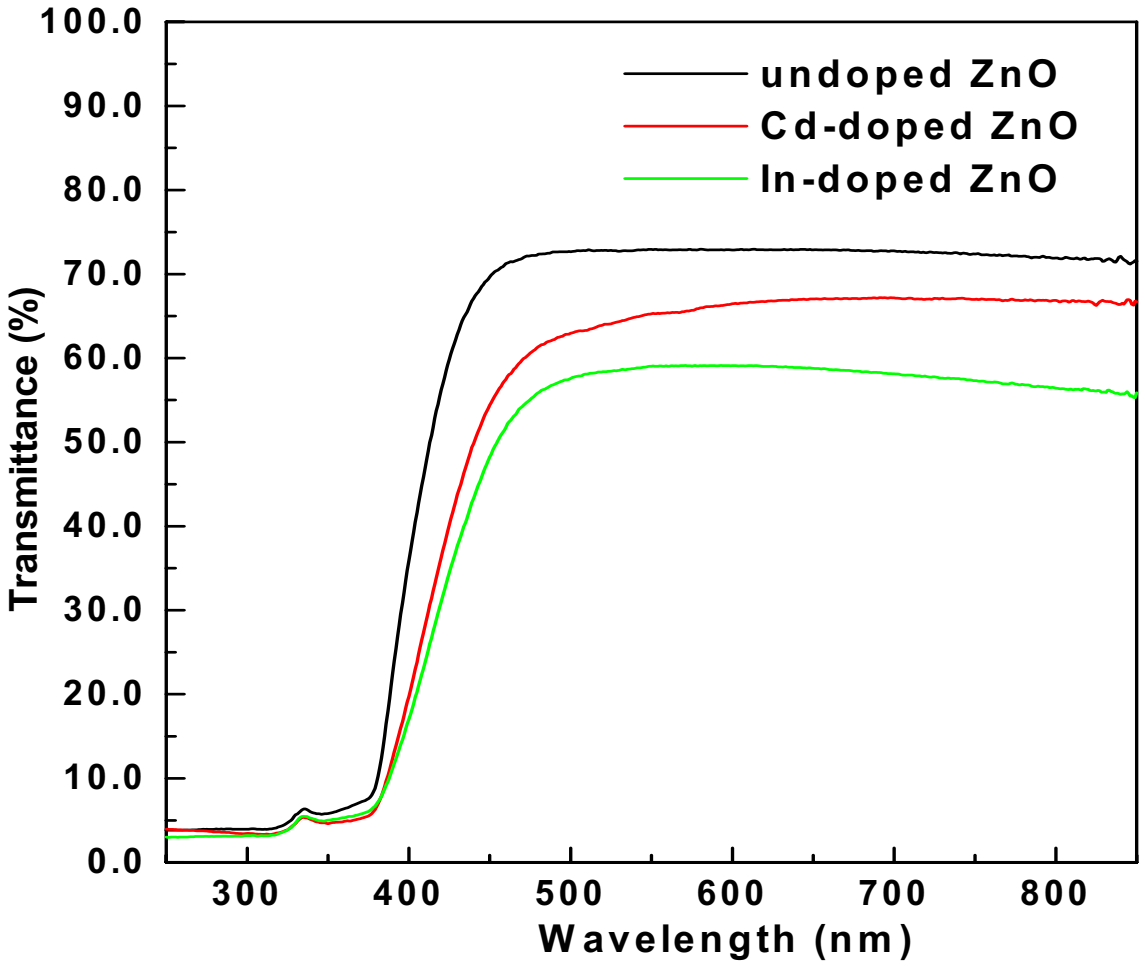

Figure 3.18 UV-visible diffuse reflectance spectra for undoped, Cd-doped and In- doped ZnO samples.

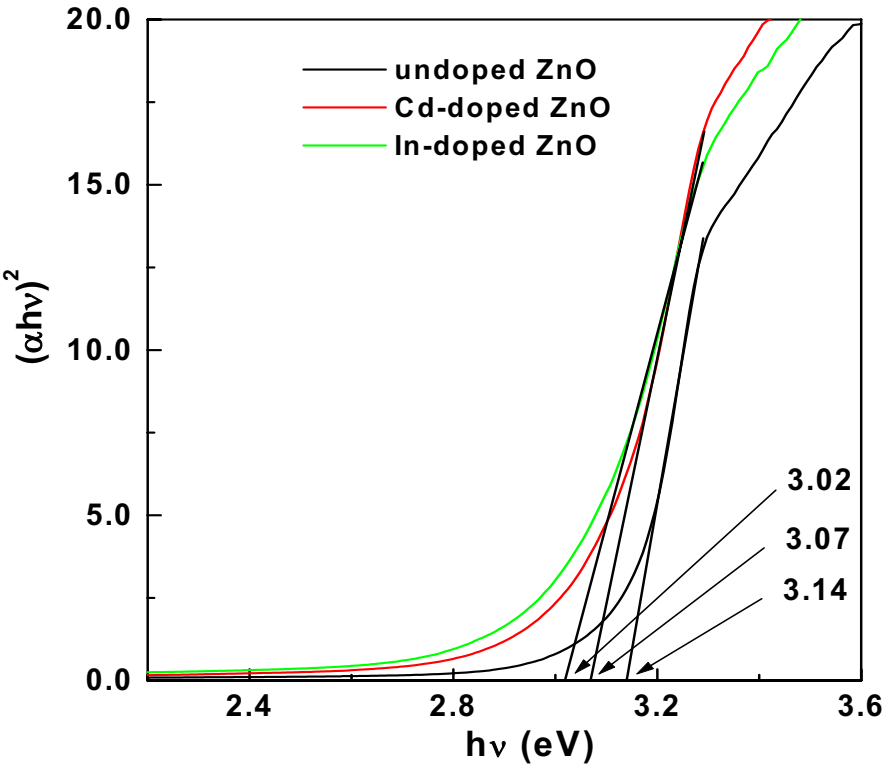

Figure 3.19 Tauc plots for undoped, Cd-doped and In-doped ZnO samples. α is the absorption coefficient computed as a function of the energy (hν) from the UV-visible diffuse reflectance data in Fig. 3.18.

Photoelectrochemical behavior

Figure 3.20 contains photoaction spectra for the undoped, Cd-doped, and In-doped ZnO samples in 0.5 M Na_2SO_4 supporting electrolyte. These spectra were acquired at a bias potential of 0.34 V. Clearly, the doped samples show a superior photoresponse to undoped ZnO over the entire wavelength range from ~300 nm to ~ 450 nm. The shift of the band edge cut-off to longer wavelengths (lower energies) for the two doped samples, relative to undoped ZnO, is also entirely consistent with the trends seen earlier in Fig. 3.19. Doping of ZnO with either Cd or In clearly results in visible light sensitization of the parent oxide.

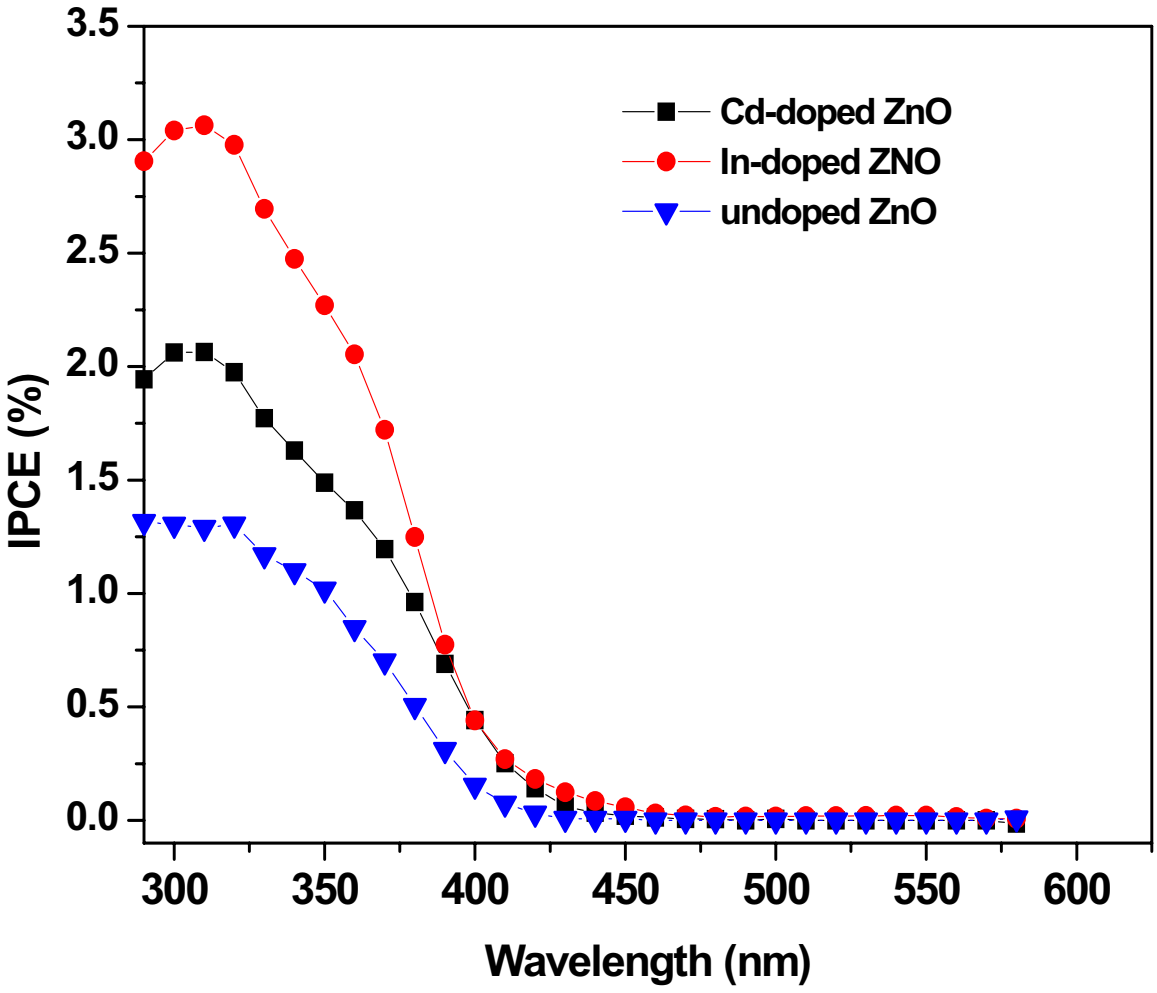

Figure 3.20 Photoaction spectra of undoped, Cd-doped, and In-doped ZnO in 0.5 M Na_2SO_4. The spectra were acquired at 0.34 V; IPCE stands for incident photon-to-electron conversion efficiency.

CHAPTER 4

DISCUSSION

4.1 Electrodeposition of Cd-doped ZnO

A detailed discussion of the results of a previous study [44] which was carried out under similar conditions with electrochemical baths having the same chemical compositions but at a more negative potential (-950 mV) is beyond the scope of this text. Essentially, electrodeposition under those conditions resulted in the formation of mixed $(ZnO)_x(CdO)_{1-x}$ films. However, it is evident from the analyses described in the preceding chapter, that at the more positive potential, Cd-doped ZnO films can be secured. Presumably, the more negative potential (-0.950 V) induces film deposition at such a fast rate that Cd incorporation into the ZnO structural framework does not occur. As a corollary, at the more positive potential (-0.725 V) where free Cd deposition cannot (and did not) occur, the remaining modes of Cd assimilation from the electrolyte by the growing film, are either as $Cd(OH)_2$ (as a separate phase which is subsequently thermally converted to CdO in the anneal step [37]) or as Cd ionic species doped into the ZnO lattice.

The Hume-Rothery solid solubility rules [39] provide empirical predictive guidelines for whether CdO dissolves in ZnO. Table 4.1 compares the solubility criteria versus the properties of CdO and ZnO and the constituent metallic components, Cd and Zn. While two of the criteria are not met, two others are satisfied. It must be noted that

all the Hume-Rothery rules are not always applicable for all pairs of elements which do show complete solubility [39].

While mixed ZnO-CdO films are formed by the sol-gel [16] and spray-pyrolytic [17-19] processes, many of the other preparative methods identified in an introductory paragraph above [20-24, 38] do afford alloyed films. The extent of alloying reported does vary and ranges from y = 0.07 [20] to y = 0.697 [24] (y is the Cd content in the formula $Cd_yZn_{1-y}O$). However, phase separation has been observed at high levels of CdO content (see for example, Refs. 21 and 22). Nonetheless, all these reported levels are well above the thermodynamic solid solubility limits.

On the other hand, the films obtained at -0.725 V consist of ZnO doped with Cd up to a level of y = 0.025 (Figure 3.8). This rather low level (compared with the values of y above) is consistent with doping of ZnO rather than alloying. The corresponding bandgap shift observed (Figure 3.6) of ~0.17 eV at y = 0.025 may be compared with ~0.16 eV for y = 0.16 [38], ~0.80 eV for y = 0.33 [20], 1.4 eV for y = 0.697 [24] and ~0.80 eV for y = 0.78 [22] observed in previous studies. Obviously the E_g shift secured is very dependent on the particular method used for film preparation.

Finally, the improved photoresponse seen in Figures 3.10 and 3.11 for Cd-doped ZnO samples is consistent with their lowered bang gaps and enhanced grain sizes relative to pure ZnO. A higher grain size translates to a lower extent of recombination and hence a better photoresponse- a trend that is well established in the solid-state photovoltaics community. Thus the data in Figures 3.10 and 3.11 underline the beneficial effect of Cd-doping of ZnO from a device application perspective.

Table 4.1 Comparison of Hume-Rothery criteria (for appreciable solid solubility) and characteristics of the Zn-Cd-O ternary system and the constituents

Criterion	Whether obeyed in the Zn-Cd-O system	Comments
Crystal structure must be the same.	no	ZnO has a hexagonal (wurtzite) structure while CdO crystallizes in the cubic fcc system.
Must belong to the same group in the Periodic Table and have the same valence.	yes	Both Zn and Cd belong to the same group.
Must have comparable atomic or ionic radii varying by less than ~15%.	no	Zn^{2+} and Cd^{2+} have ionic radii of 0.088 nm and 0.109 nm respectively (a ~23% difference).
Electronegativities of the two elements must be comparable.	yes	The Zn and Cd electronegativities on the Pauling scale (1.65 and 1.69 respectively) are comparable.

4.2 Combustion Synthesis of Cadmium- and Indium-doped ZnO

One of the most significant results emerging from this study is that the use of a chloride precursor in combustion synthesis for introducing cadmium as a dopant into the zinc oxide lattice avoids problems associated with phase separation as in the nitrate precursor case. As with regard to the In-doped ZnO, since indium nitrate was not used as a precursor, the formation of $(ZnO)_mIn_2O_3$ polytypes (materials that have already been studied extensively) was avoided. Thus both Cd-doped and In-doped ZnO samples were successfully prepared by combustion synthesis using $CdCl_2$ and $InCl_3$ precursors. The data from the present study on Cd- and In-doped ZnO samples from combustion synthesis are now discussed in the light of corresponding data trends in the literature.

The decrease in particle size on doping (as assessed by XRD data analyses) is consistent with the findings from a recent study on In-doped ZnO thin films using spray pyrolysis [15]. These authors also observed an increase in the FWHM of the XRD peaks for (002) and (101) reflections, consistent with our own observations on the (100) (and the other XRD) peaks in this study. Indium doping levels ranging from 0.005 to 0.05 were reported in the aforementioned study. On the other hand, our assays of the Cd and In dopant levels via EDX far exceed the estimates obtained from the XRD peak shifts. Taking into consideration the fact that Cd and In solution doses in the initial combustion mixture were 0.06 (atom ratio) in each case and that the thermodynamic solid solubility limit for impurities in the ZnO lattice is ~2%, we can conclude that the dopant levels in the ZnO lattice are significantly lower. The higher Cd and In levels seen by the XPS and EDX probe possibly translate to a preferential migration of the dopants to the ZnO surface thus forming an amorphous grain boundary phase. This is consistent with the

observations made by other authors [40]. The discrepancy in the Cd and In assays between the EDX and XPS is easily rationalized when one recalls the very different sampling depths inherent in the two techniques; i.e., the XPS probe samples the surface rather than the bulk unlike EDX. Note that the photoelectron escape depth is only ~2 nm while the X-ray escape depth is ~2 μm.

The shrinking of the bandgap on Cd doping is consistent with the trend seen by other authors [20]. On the other hand, in a previous study using spray pyrolysis[15], only a "slight" increase in E_g (from 3.3 eV to 3.33 eV) was reported on In-doping. Much more sizeable increases in E_g (from 3.27 eV to 3.42 eV) were noted on In-doped ZnO samples prepared by electrodeposition [40]. On the other hand, Li^+-ion doping of ZnO decreased the E_g value from 3.2 eV to 3.1 eV while Ga-doping of ZnO thin films (as prepared by plasma-enhanced metal organic chemical vapor deposition) increased the E_g value from ~3.25 eV to ~3.55 eV [35].

The E_g variation with In-doping of ZnO can be explained in terms of the resultant perturbation in the carrier concentration in the conduction band. When ZnO is doped with a Group III element such as In, the dopant presumably acts as a singly-charged donor by substituting for Zn. The excess carriers furnished by the dopant impurity in the conduction band (after ionization) contribute to a blue-shift of the optical band-to-band transition (the so-called Burstein-Moss effect) [41]. However, when the carrier concentration in the conduction band of the host exceeds a critical threshold (in this case, 5×10^{19} cm^{-3}) band-gap *narrowing* becomes significant because of: (a) merging of donor and conduction band energy levels; (b) band-tailing by impurity induced potential fluctuations; and (c) electron-electron and screened electron-ion many-body contributions

to the electron and hole self energies. This “anomalous” effect was seen for n-type In-doped ZnO films by other authors [42] and the shrinking of E_g observed in our study for doping of ZnO with In or Cd is attributed to a similar effect.

CHAPTER 5

CONCLUDING REMARKS

In summary, Cd-doped ZnO thin films were successfully electrodeposited from oxygenated baths containing varying amount of Zn^{2+} and Cd^{2+} species using the cathodic base electrogeneration approach. The Cd-doped ZnO samples were found to show a superior photoresponse relative to undoped ZnO. Further efforts could be directed towards a fuller understanding of the sensitivity of the film composition to the deposition potential as well as the deposition mechanism itself.

This study also demonstrated that combustion synthesis can be useful for preparing doped ZnO powders with vastly improved photoresponses relative to the undoped samples. The use of metal chlorides (instead of the commonly-used metal nitrate salts in combustion synthesis) as dopant precursors was found to facilitate dopant incorporation into the ZnO lattice. The properties of the doped powders need to be studied in further detail and material parameters such as the degree of dopant incorporation, carrier concentration and mobility need to be ascertained.

REFERENCES

[1] M. Joseph, H. Tabata, and T. Kawai, Jpn. J. Appl. Phys. 38 (1999) L 1205.

[2] C. Klingshirn, R. Hauschild, H. Priller, M. Decker, J. Zeller, and H. Kalt, Superlattices and Microstructures 38 (2005) 209.

[3] N. H. Nickel and E. Terukov, Zinc Oxide-A Material of Micro- and Optoelectronic Applications, Springer, AA Dordrecht, The Netherlands, 2005.

[4] C.R. Gorla, N.W. Emanetoglu, S. Liang, W. E. Mayo, Y. Lu, M. Wraback, and H. Shen, J. Appl. Phys. 85 (1999) 2595.

[5] H.Z. Wu, K.M. He, D.J. Qiu, and D.M.Huang, J. Cryst. Growth 217 (2000) 131.

[6] H. Nanto, T. Minami, S. Shooji, and S. Takata, J. Appl. Phys. 5 (1984) 1029.

[7] Z.-C. Jin, I. Hamberg, and C. G. Granqvist, J. Appl. Phys. 64 (1988) 5117.

[8] C.E. Rice, G.S. Tompa, L.G. Provost, N. Sbrockey, and J.D. Cuchiaro, Mat. Res. Symp. Proc. 764 (2003) 117.

[9] S. Peulon and D. Lincot, J. Electrochem. Soc. 145 (1998) 864.

[10] Q. Wan, Q.H. Li, Y.J. Chen, T.H. Wang, X.L. He, X.G. Gao, and J.P. Li, Appl. Phys. Lett., 84 (2004) 3085.

[11] T.K. Gupta, J. Am. Ceram. Soc. 73 (1990) 1817.

[12] H. Kasper, Z. Anorg. Allg. Chem. 349 (1967) 113.

[13] S. Kikkawa, S. Hosokawa, and H. Ogawa, J. Am. Ceram. Soc. 88 (2005) 308.

[14] T.Minami, H. Sonohara, T. Kakumu, and S. Takata, Jpn. J. Appl. Phys. 34 (1995) L 971.

[15] P.M.R. Kumar, C.S. Kartha, K.P. Vijayakumar, T. Abe, Y. Kashiwaba, F. Singh, and D.K. Avasthi, Semicond. Sci. Technol. 20 (2005) 120.

[16] Y.-S. Choi, C.-G. Lee, and S.M. Cho, Thin Solid Films 289 (1996) 153.

[17] O. Vigil, F. Cruz, G. Santana, L. Vaillant, A. Morales-Acevedo, and G. Contreras-Puente, Appl. Surf. Sci. 161 (2000) 27.

[18] O. Vigil, L. Vaillant, F. Cruz, G. Santana, A. Morales-Acevedo, and G. Contreras-Puente, Thin Solid Films 361-362 (2000) 53.

[19] H. Tabet-Derraz, N. Benramdane, D. Nacer, A. Bouzidi, and M. Medles, Solar Energy Mater. Solar Cells 73 (2002) 249.

[20] T. Makino, Y. Segawa, M. Kawasaki, A. Ohtomo, R. Shiroki, K. Tamura, T. Yasuda, and H. Koinuma, Appl. Phys. Lett. 78 (2001) 1237.

[21] K. Sakurai, T. Takagi, T. Kubo, D. Kajita, T. Tanabe, H. Takasu, S. Fujita, and S. Fujita, J. Cryst. Growth 237-239 (2002) 514.

[22] D.W. Ma, Z.Z. Ye, J.Y. Huang, L.P. Zhu, B.H. Zhao, and J.H. He, Mater. Sci. Eng. B111 (2004) 9.

[23] Q. Wan, Q.H. Li, Y.J. Chen, T.H. Wang, X. L. He, X.G. Gao, and J.P. Li, Appl. Phys. Lett. 84 (2004) 3085.

[24] A. Nakamura, J. Ishihara, S. Shigemori, K. Yamamoto, T. Aoki, H. Gotoh, and J. Temmyo, Jap. J. Appl. Phys. 44 (2005) L4.

[25] R.K. Pandey, S.N. Sahu, and S. Chandra, Handbook of Semiconductor Electrodeposition, Marcel Dekker, New York, NY, 1996.

[26] N.L. Weinberg, J. Chem. Ed. 60 (1983) 268.

[27] T. Nohira, K. Yasuda, and Y. Ito, Nat. Mater. 2 (2003) 397.

[28] L. E. Griffiths, M. R. Lee, A. R. Mount, H. Kondoh, T. Ohta, and C. R. Pulham, Chem. Commun. (Cambridge) (2001) 579.

[29] I.M. Dharmadasa, and J. Haigh, J. Electrochem. Soc. 153 (2006) G47.

[30] T. Pauporte, and D. Lincot, J. Electroanal. Chem. 517 (2001) 54.

[31] D. Lincot, Thin Solid Films 487 (2005) 40.

[32] K.C. Patil, S.T. Aruna, and S. Ekambaram, Curr. Opin. Solid State Mater. Sci. 2 (1997) 158.

[33] V.C. de Sousa, M.R. Morelli, and R.H.G.A. Kiminami, Int. J. Self-Propag. High-Temp Synth. 7 (1998) 327.

[34] C-C. Hwang, and T-Y. Wu, J. Mater. Sci. 39 (2004) 6111.

[35] F. Gu, S.F. Wang, M.K. Lü, G.J. Zhou, D. Xu, and D.R. Yuan, Langmuir 20 (2004) 3528.

[36] V.C. de Sousa, M.R. Morelli, and R.H.G.A. Kiminami, Ceram. Int. 26 (2000) 561.

[37] A. Seshadri, N.R. de Tacconi, C.R. Chenthamarakshan, and K. Rajeshwar, Electrochem. Solid-State Lett. 9 (2006) C1.

[38] F. Wang, H. He, Z. Ye, L. Zhu, H. Tang, and Y. Zhang, J. Phys. D: Appl. Phys. 38 (2005) 2919.

[39] W.F. Smith, Foundations of Materials Science and Engineering, McGraw-Hill, New York, 1993, p. 377.

[40] G. Machado, D.N. Guerra, D.Leinen, J.R. Ramos-Barrado, R.E. Marotti, and E.A. Dalchiele, Thin Solid Films 490 (2005) 124.

[41] E. Burstein, Phys. Rev. 93 (1954) 632.

[42] K.J. Kim, and Y.R. Park, Appl. Phys. 78 (2001) 474.

[43] S.R. Jain, K.C. Adiga, and V.R. Pai Verneker, Combust. Flame 40 (1981) 71.

[44] A. Seshadri, Masters Thesis, The University of Texas at Arlington, 2005.

BIOGRAPHICAL INFORMATION

The author received his Master of Science in Materials Science and Engineering from The University of Texas at Arlington in August 2006. He received his Bachelor of Technology in Chemical engineering from Anna University in June 2004.